RESEARCH ARTICLE

WILEY

Influence of forest canopy structure and wind flow on patterns of sub-canopy snow accumulation in montane needleleaf forests

Jacob Staines | John W. Pomeroy 🅾

Centre for Hydrology, University of Saskatchewan, Canmore, Canada

Correspondence
John W. Pomeroy, Centre for Hydrology, University of Saskatchewan, Canmore, Canada.
Email: john.pomeroy@usask.ca

Abstract

Vegetation structure is considered one of the most important factors shaping the spatial variation of snow accumulation under forest canopies. However, fine scale relationships between canopy density, snow interception, wind redistribution and sub-canopy accumulation are poorly understood and difficult to observe, and their influence governing stand-scale snow distributions that determine snow covered area depletion during melt is largely unknown. In this study, fine-scale observations of forest structure and sub-canopy snow accumulation were analysed over two mid-winter snowfalls to a sub-alpine forest in Marmot Creek Research Basin, Canadian Rockies, Alberta, to identify the impact of snow-canopy interactions on spatial patterns of sub-canopy snow accumulation. High spatial resolution (5 and 25 cm) snow accumulation estimates and canopy structure metrics were calculated from the combination of repeated UAV-lidar observations with snow and photographic surveys, utilizing novel resampling methods including voxel ray sampling of lidar (VoxRS) to improve metric robustness and reduce bias. Over 50% of the spatial variance in forest snow accumulation was found at length scales less than 2 m, supporting the role of local scale canopy structure in governing variation in subcanopy snow accumulation. Additionally, subcanopy snow accumulation showed significant angular spread in relationships with overhead canopy structure; the vertical asymmetry coinciding with local windflow directions during snowfall. Detailed angular analysis showed nontrivial snow-vegetation relationships that likely reflect multiple snowfall-vegetation processes, including unloading and entrainment of intercepted snowfall during wind gusts and funnelling of entrained particles by downwind vegetation. These fine-scale findings suggest several emergent processes which may influence snow accumulation at the scale of forest stands, with novel considerations for representing snow water equivalent distributions under dense evergreen canopies under varying environmental and canopy conditions. Similar studies over a broad range of conditions and forests will help refine and generalize the effects observed here for further snow hydrology and forestry applications.

KEYWORDS
canopy structure, forest snowpack, lidar, snow accumulation, snow interception, voxel ray sampling

1 | INTRODUCTION

Vegetation structure is one of the most important factors controlling the spatial and temporal variation of snow in forests over length scales of less than 1000 m (Deems & Painter, 2006; Zheng et al., 2015), with dominant length scales of variation typically observed within 40 m (Clark et al., 2011; Pomeroy et al., 2002; Shook & Gray, 1997; Trujillo et al., 2007). This is due in part to the roles of vegetation in altering snow accumulation, interception, redistribution and ablation processes (Musselman et al., 2008; Varhola et al., 2010). Spatial distributions of snow as shaped by vegetation go on to determine snow cover depletion rates during melt periods, driving ablation rates and contributing areas for snowmelt runoff (Clark et al., 2011; DeBeer & Pomeroy, 2010; Faria et al., 2000). Vegetation structure therefore impacts both quantity and timing of snowmelt runoff in forested basins with seasonal snowpacks (Dickerson-Lange et al., 2017).

Changes in vegetation structure drive significant changes in hydrology in cold regions due to the coupling of vegetation structure and snow accumulation processes (Varhola et al., 2010). Vegetation loss can result in reduced snow interception and sublimation and therefore greater accumulation on the ground following forest loss due to wildfire, insect infestation, disease and clearcutting, followed by significant increases in ablation rates during melt periods (Ellis et al., 2013; Harpold et al., 2014; Musselman et al., 2008; Pomeroy & Goodison, 1997; Pomeroy & Granger, 1997; Pomeroy et al., 2012). These findings have inspired efforts to alter forest structure by selective thinning to increase snowmelt runoff quantities, with mixed results (Golding & Swanson, 1978; Harpold et al., 2020; Troendle & Leaf, 1981). Such changes in vegetation structure affect local and downstream hydrology with ramification for ecosystems and human systems alike (Broxton et al., 2015; Trujillo et al., 2012). Land management, ecological conservation and water resource decisions therefore need to be informed by robust understandings of snow-vegetation interactions, particularly in the contexts of unprecedented global climate change, increasing forest disturbance, and ongoing deforestation and land use change (Curtis et al., 2018; Johnston et al., 2020; Volney & Fleming, 2000).

Efforts to model snow accumulation and interception in forests have yielded many independent parameterizations of interception processes as functions of canopy metrics (e.g. Andreadis et al., 2009; Hedstrom & Pomeroy, 1998; Moeser, Stähli, & Jonas, 2015; Roth & Nolin, 2019; Schmidt & Gluns, 1991). Enduring differences in the canopy metrics and parametrizations used in models suggest that further validation is needed to determine the advantages and limitations of various assumptions when applied to disparate environments and conditions (Clark et al., 2011; Lundberg & Halldin, 2001; Rutter et al., 2009). As most canopy metrics are calculated from angular or spatial aggregations of canopy structure, a given metric's use in parametrizing forest snow accumulation represents an assumption about which parts of the canopy over a given point are relevant to the local accumulation of sub-canopy snow. Even within

a given class of canopy metrics (e.g. leaf area index, canopy height), there are varying assumptions regarding what spatial or angular footprints are used (Varhola & Coops, 2013). While sub-canopy radiation regimes are usually parametrized by canopy metrics with carefully selected angular footprints (e.g. Mazzotti, Essery, Webster, et al., 2020), limited validation of angular footprints of snow-vegetation interactions leave model developers uninformed about optimal canopy metric selection when parametrizing forest snow accumulation models. High-resolution observations of angular and spatial relationships between canopy vegetation and sub-canopy snow accumulation could inform not just modelling decisions but also a deeper understanding of the physical snow accumulation processes driving these relationships, which such models are designed to describe (Clark et al., 2017).

Forest snow accumulation processes such as interception and unloading can occur rapidly and at length scales from that of individual snowflakes to trees. Process interactions and outcomes are highly complex and are unrealistic to explicitly model at larger spatial and temporal scales. Instead, aggregate effects of these processes are more appropriately described in terms of emergent processes observed at the scales of forest stands and storms (Newman et al., 2019). Such emergence in forests presents opportunities to characterize complex systems of branches using much simpler models that use aggregate canopy characteristics and storm totals to model snow interception, or solar angles and leaf area index (LAI) for shortwave radiation transmittance (Hedstrom & Pomeroy, 1998; Moeser, Stähli, & Jonas, 2015; Nilson, 1971; Pomeroy & Dion, 1996). More research is needed to understand the dependence of emergent processes of snow accumulation in forests on environmental conditions and canopy structure (Huerta et al., 2019) – to characterize relevant length scales and to determine caveats and corrections for future models without reliance on assumptions of spatial and temporal stationarity in canopy properties or environmental conditions.

Carefully characterizing the angular and spatial effects of forest canopies on sub-canopy snow accumulation can help to link stand-scale variability in canopy density to variability in snow accumulation. The purpose of this study is to identify dominant angular and spatial footprints of snow-vegetation interactions in patterns of subcanopy snow accumulation, achieved through the following three objectives:

1. measure and describe the distributions of snow and canopy structure at high spatial resolutions,
2. determine length scales of variation of snow and canopy structure, and
3. determine the angular footprint of canopy effects on snow accumulation.

This study utilizes recent advances in UAV-lidar technology alongside novel resampling methods to characterize vegetation structure and surrounding snow accumulation within a forest stand at high spatial resolutions (Harder et al., 2020).

2 | DATA AND METHODS

2.1 | Study site and period

This study was conducted within Marmot Creek Research Basin, on the eastern slope of the Canadian Rockies, Alberta, Canada (Fang et al., 2019). The study site (Figure 1a) includes the instrumented "Upper Forest" and "Upper Clearing" research sites (Pomeroy et al., 2012; Musselman et al., 2015), comprising 2.51 ha of secondary growth forest with an average elevation of 1829 m above mean sea level and mean slope of 7° to the NE. Vegetation consisted primarily of Engelmann spruce (*Picea engelmannii*), subalpine fir (*Abies lasio-carpa*), and lodgepole pine (*Pinus contorta var. Latifolia*), with an average stem density of ~6000 stems ha^{-1} within the forest. The site contains several clearings which were logged in the 1970s for a forest hydrology experiment (see Rothwell et al., 2016) and which have since seen partial juvenile regrowth (Figure 1b). Two plots were established within the study site for analysis: the "forest" plot and "clearing" plot (red and yellow paths in Figure 1a, respectively).

An array of instruments across the site recorded meteorological and hydrological conditions at 15-min time intervals (see Fang et al., 2019 for a full description of instrumentation and for published datasets). This study used observations from the Upper Forest and Upper Clearing meteorological stations located within the forest and clearing plots (Figure 1b) including air temperature, relative humidity, wind speed and direction, and snow depth time series. Also used were air temperature, wind speed, and direction from the Upper Clearing meteorological tower, with sensors located 17 m above the ground (AGS). Cumulative precipitation within the clearing was measured with a Geonor T200B with Alter shield, corrected for snowfall undercatch following Smith (2007). Snow depth time series were collected using SR50 acoustic sensors, corrected for speed of sound fluctuations with air temperature (Campbell Scientific Canada, 2009) and smoothed using a 3.25 h moving average with symmetric, odd-length kernel to minimize noise prior to analysis (Ryan et al., 2008).

This study focuses on the 7-day study period from February 14 to 21, 2019, during which two distinct storms passed over the site (Figure 2). Three surveys were conducted within the study period (Table 1)—one each before, between, and after the two storms—resulting in two time intervals referred to chronologically as "Storm 1" and "Storm 2". Each survey consisted of an aerial UAV-lidar component followed by ground-based snow and hemispherical photography surveys. Air temperatures within the forest ranged from −23 to −8°C over the study period, with relative humidity near saturation. Wind speeds were lower for Storm 1, with a median 17 m AGS wind speed of 0.34 m s^{-1} compared with 0.45 m s^{-1} for Storm 2. The azimuths of the mean 17 m AGS wind vectors were 136° and 125° (clockwise from north) for storms 1 and 2 (see Figure 3). Wind speeds within the forest (2.77 m AGS) reached maximum values of 0.21 and 0.78 m s^{-1} with median values of 0.0 and 0.108 m s^{-1} for storms 1 and 2, respectively. Intercepted snow was observed in the canopy over the extent of the study period.
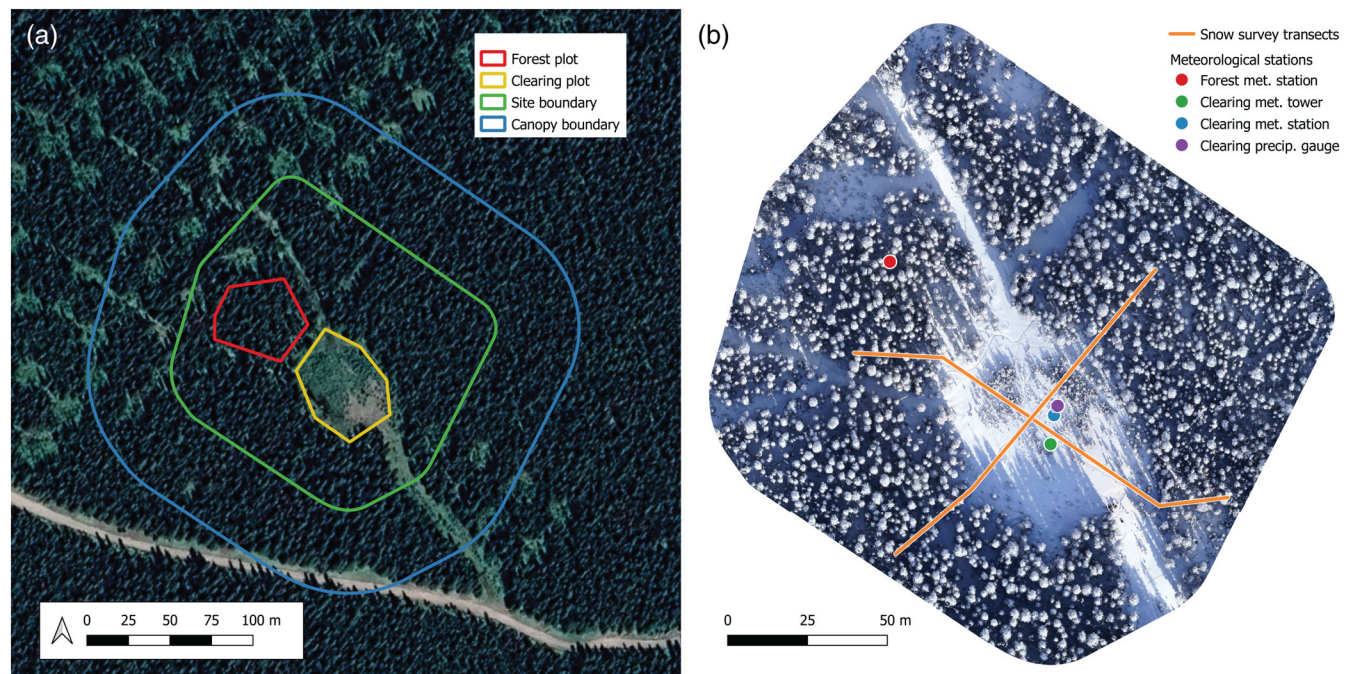
FIGURE 1 (a) Site overview from satellite imagery showing the extent of the research area and plots. Lidar-derived snow metrics were calculated over the extent of the site boundary (green). Canopy structure analysis considered vegetation up to 50 m away from each ground point (outermost canopy boundary shown in blue). Plot-specific analysis was conducted separately for each of the forest (red) and clearing (yellow) plots. (b) An orthomosaic over the site boundary generated from UAV photography from 21 February 2019 and compiled using structure from motion with the Pix4D software (v. 4.6.2). Locations of snow survey transects and meteorological stations within the site are overlaid.
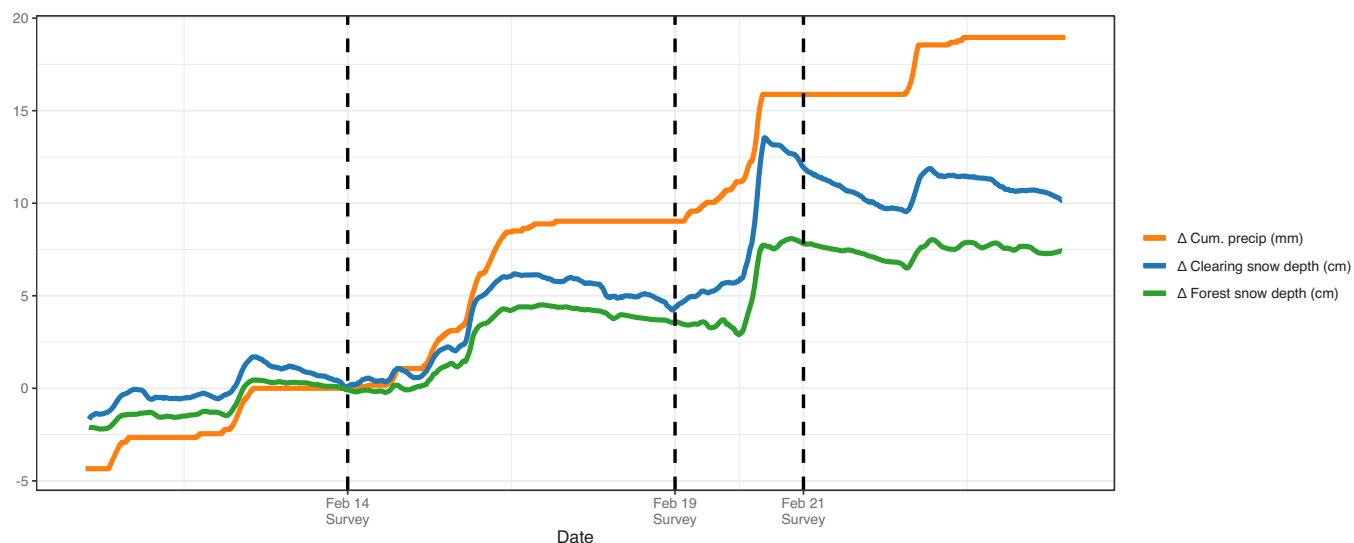
FIGURE 2 Changes in cumulative precipitation in the clearing and snow depths in the clearing and forest over the study period relative to the first survey (February 14). Dashed vertical lines correspond to the three survey dates within the study period. Two storms passed over the site within the study period which were each bounded by surveys: Storm 1 (February 14–19), and Storm 2 (February 19–21).

TABLE 1 Survey dates and corresponding snow observations.

| Date	Day of year	UAV survey end time	Cumulative clearing precipitation SWE (mm)	Clearing SR50 snow depth (cm)	Forest SR50 snow depth (cm)	Clearing snow density intercept b_c (kg m^{-3})	Clearing snow density slope m_c (kg m^{-4})	Forest snow density constant ρ_f (kg m^{-3})
14 February 2019	045	12:55	171	57.0	32.8	109	1.27	165
19 February 2019	050	12:41	180	60.9	36.4	118	1.09	159
21 February 2019	052	11:40	187	68.4	40.6	76.7	1.44	134
29 May 2019	145	11:54	326	0	0	n/a	n/a	n/a

Note: Cumulative precipitation measured by the precipitation gauge is reported from 1 October 2018. A linear snow density–depth relationship was assumed for the clearing plot with slope and intercept values shown, while an average density was assumed within the forest plot, for each day. The final survey on 29 May 2019 was used for reference of the snow-free ground surface.

2.2 | UAV-lidar data collection and processing

A total of four pre-programmed UAV-lidar surveys were conducted over the field site: three during the February 2019 study period, and one on 29 May 2019 to measure the bare ground surface and the canopy under "snow-off" canopy conditions (see Table 1). Lidar observations were collected using a RIEGL miniVUX-1 UAV-lidar sensor and integrated Applanix APX-20 inertial measurement unit (IMU), mounted on a DJI M-600 Pro uncrewed aerial vehicle (UAV) with global navigation satellite system (GNSS) for georeferencing (see Harder et al., 2020 for detailed platform specifications). The lidar sensor uses a laser beam with a wavelength of 905 nm and a primary-axis beam divergence of 1.6 mrad. A 45° rotating mirror results in a 360° cylindrical scanning pattern with the axis of rotation parallel to the flight path. Lidar samples were collected at a rate of 100 kHz with a

mirror rotation speed of 50 Hz. The miniVUX-1UAV conducts onboard processing of the lidar waveforms to produce a discrete-return output with up to five returns per shot. The combined system results in a horizontal accuracy of <5 cm and a vertical accuracy of <10 cm for individual lidar returns (Harder et al., 2020). A co-registered Sony a6000 RGB camera collected aerial photographs of the canopy and ground every 2 s. Each UAV-lidar survey consisted of three 10-to-15-minute pre-programmed flight paths, ranging in elevation from 40 to 120 m AGS to survey the site from several different perspectives. Flight paths were designed and executed using the UgCS flight control software (SPH Engineering, 2020).

Lidar, IMU, and GNSS observations were integrated into georeferenced lidar point clouds following the workflow from Harder et al. (2020). Post-processed UAV flight trajectories were generated by reconciling IMU data with GNSS observations, enhanced with
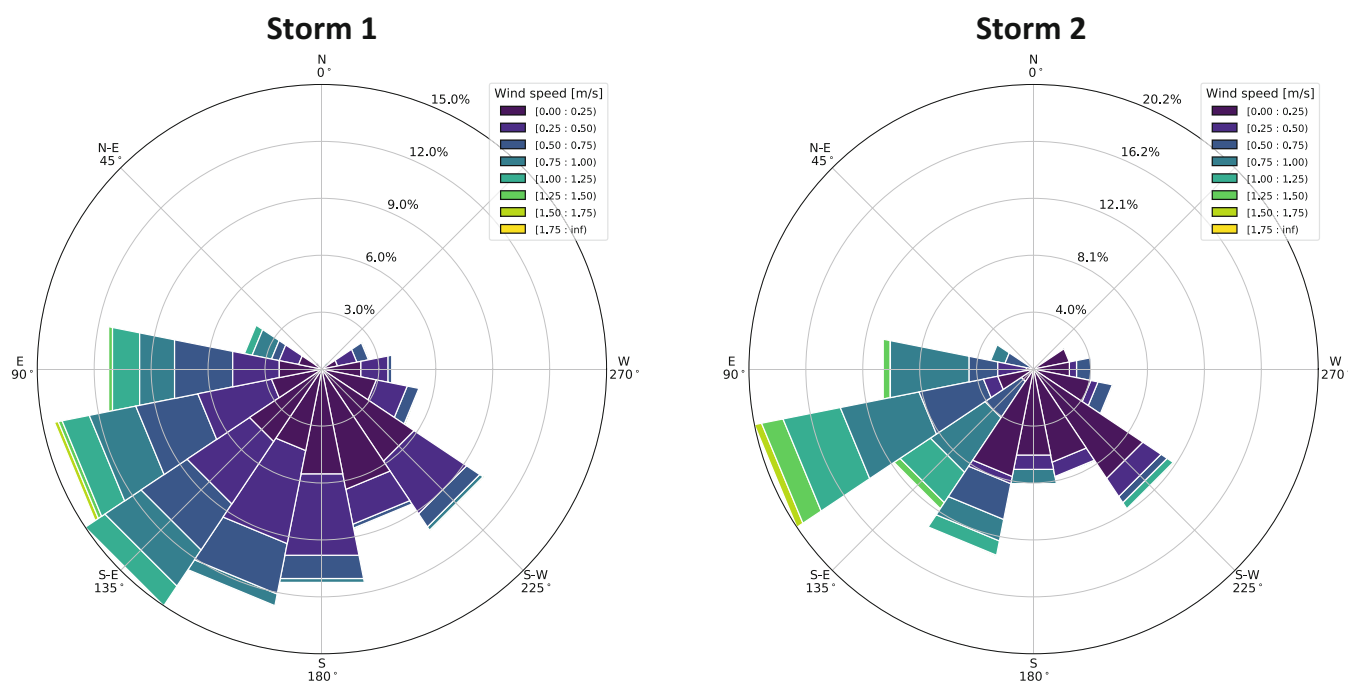
FIGURE 3 Normalized histograms of wind speed (m s^{-1}) and wind direction (° clockwise from north, upward looking) over the storm 1 (a) and storm 2 (b) observation periods. Plots use the upward-facing (flipped east-to-west from the conventional downward-facing perspective) to simplify visual comparison with hemispherical analysis in Figures 4 and 11.

PPP-corrected differential GNSS observations (Natural Resources Canada, 2021) using the POSPac UAV software. Lidar return point clouds were then converted from a sensor-referenced to georeferenced frame using the RIEGL RiPROCESS software.

The georeferenced lidar point clouds from each survey day were subject to quality control measures and surface and vegetation return classification using the LAStools software package (Isenburg, 2020). Point clouds were cropped to the site boundary delineated by a 15 m horizontal buffer of the outermost flight path for ground analysis, and to the canopy boundary delineated by a 65 m buffer for canopy analysis (green and blue paths in Figure 1a, respectively). Duplicate points were removed. Returns with no neighbours within the surrounding 1 m^3 cube were flagged as noise and removed. Surface returns (ground or snowpack) were identified from the subset of last returns using the Lastools "lasground_new" function with a step size of 0.5 m and an offset of 0.1 m, removing upward and downward spikes greater than 0.1 m. Returns with elevations within 0.05–35 m AGS were classified as "vegetation". Processed point clouds yielded a mean return density of 3860 returns m^{-2} over the forest plot, with an average of 3090 first returns m^{-2}. Snow and ground surface return densities were highly spatially variable within the forest, with an average of 839 surface returns m^{-2}.

2.3 | Snow surveys

1. Manual snow surveys were conducted following each UAV survey to validate aerial observations and drive snow density models.

Snow surveys were conducted along two perpendicular transects originating and terminating in the forest and traversing the clearing plot (Figure 1b). A minimum of 20 clearing and 20 forest snow depth samples were collected at 2.5 m intervals along the flagged transects for each survey. Snow water equivalent (SWE) measurements were taken with an ESC-30 snow tube at every other snow depth sample point, where snow depth exceeded 20 cm. Snow depth and SWE sample points were surveyed with a differential GNSS system where satellite signal quality permitted, for validation of LiDAR-derived snow depth and SWE estimates. Survey points had a mean 3-D coordinate quality of 1.61 cm within the clearing, and 26.6 cm within the forest.

2.4 | Hemispherical photography

Upward-facing hemispherical photographs were collected following each UAV survey using a Nikon Coolpix 4500 and EC-F8 hemispherical lens (Figure 4a), from 1.8 m AGS at 20 georeferenced points along the snow survey transects. Hemispherical photographs were visually inspected for quality, cropped to the hemispherical horizon, resized to 1000-by-1000 pixels, and thresholded manually over all RGB channels to differentiate between regions of canopy (including intercepted snow) and sky (Figure 4b). In some cases, when intercepted snow was present in the canopy view, a global threshold was insufficient to differentiate the intercepted snow from the sky, and manual darkening or lightening was applied to discrepant regions prior to thresholding. Hemispherical images were analysed in the Hemisfer software
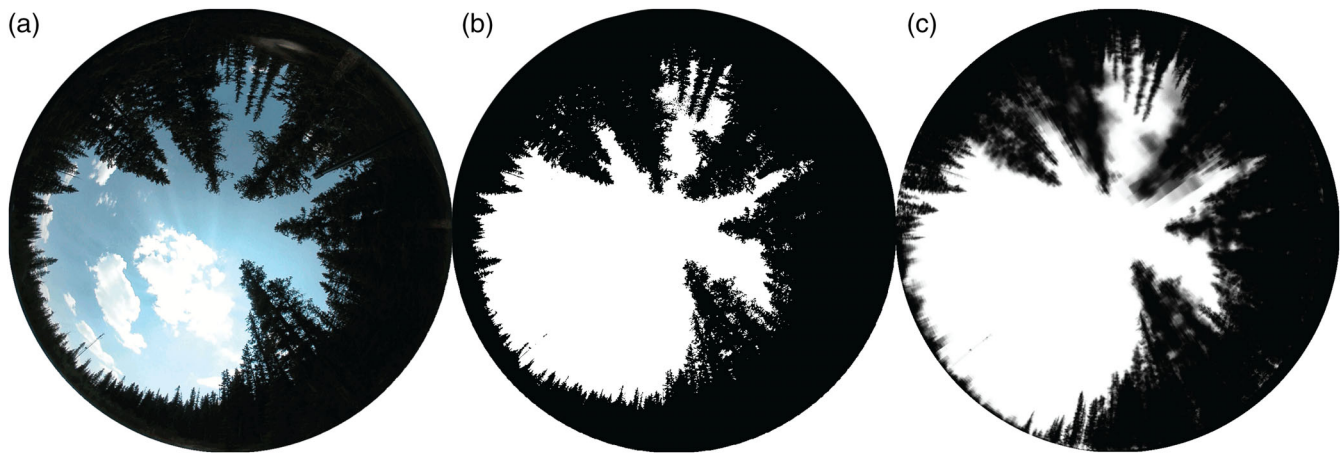
FIGURE 4 (a) An example of a cropped hemispherical photograph which was (b) thresholded for estimating canopy radiation transmittance over zenith angle bands. (c) A corresponding greyscale synthetic hemispherical image generated using voxel ray sampling of lidar (VoxRS). All images shown are 1000 × 1000 pixels and use the upward-facing hemispherical perspective, with north to the top and east to the left.

(Version 2.2, Thimonier et al., 2010) across four angle bands of 15° width spanning 0°–60° from vertical to calculate average band-wise radiation transmittance and contact numbers, weighted by within-band solid angle (Schleppi et al., 2007).

2.5 | Lidar snow products

2.5.1 | Snow depth maps

Lidar snow depth maps (HS_{lidar} [m]) were calculated for each day within the study period using a point-to-grid subtraction method (Deems et al., 2013). Each set of classified ground or snow surface returns was thinned to the finest scale of interest by selecting the surface return with the median elevation within each 5 cm × 5 cm cell, to thin dense regions and reduce the influence of vertical outliers from low-lying vegetation. A triangular irregular network (TIN) was generated from the thinned snow-free ground returns to represent the bare ground surface. The thinned snow surface returns for each survey were normalized to the height above ground by subtracting the bare ground TIN elevation at the corresponding coordinates from return elevations, yielding point clouds of snow depths from which snow depth TINs were generated. Each snow depth TIN was rasterized to resolutions of 5 cm, omitting TIN edges greater than 10 cm to limit interpolation errors. Snow depth products were then cleaned by masking regions where snow was trampled during snow surveys and two snow patches which remained in the May 29th survey, and by excluding negative values and those which exceeded the .999th quantile. A 25 cm snow depth raster was created from each 5 cm raster using a median filter.

2.5.2 | SWE maps

SWE maps for the forest (SWE_f [mm]) and clearing (SWE_c [mm]) were calculated at 5 and 25 cm resolutions from HS_{lidar} maps using separate

density models derived from corresponding snow survey observations within the forest and clearing plots, with distinctive models for each snow survey measurement day. Snow densities were modelled considering the differences between clearing and sub-canopy snow, the covariance between density and snow depth, and how they changed over time (Pomeroy & Gray, 1995). This statistical association can be due to many factors, including compaction, differences between equitemperature metamorphism of intercepted snow and temperature gradient metamorphism of sub-canopy snowpacks, impact of unloaded snow clumps, wind redistribution, melt differences and sub-canopy drip. Within the forest plot, the density of the shallow snowpack did not show a significant relationship with snow depth, consistent with the findings of Shook and Gray (1994) for snowpacks less than 60 cm in depth. Constant snow density models were therefore used to estimate SWE_f from HS_{lidar} within the forest for each survey day (Table 1). In contrast, the density of the deeper snowpack within the clearing plot did share a significant linear relationship with snow depth for two of the three surveys within the study period. This is most likely due to compaction of deeper snowpacks. SWE_c within the clearing was therefore estimated from HS_{lidar} for each day using linear models of snow density with depth (Table 1).

2.5.3 | ΔSWE maps

Maps of change in snowpack snow water equivalent (ΔSWE [mm]) over each storm interval were calculated from interval changes in lidar-measured snow depths (ΔHS_{lidar} [m]), combined with estimates of fresh snow density (ρ_{new} [mm SWE m^{-1}]) from 15-min time series of cumulative precipitation (P [mm SWE]) and acoustic snow depth (HS [m]) within the clearing. Densification of the antecedent snowpack within each storm interval was assumed to be negligible once fresh snow began to fall, such that any changes in snow depth time series between minimum (HS_{min}) and final (HS_{fin}) values within each time interval were attributed to accumulation or densification of fresh

snow only (Lv & Pomeroy, 2020). ρ_{new} at the end of each time interval was therefore estimated by:

$$\rho_{new} = \frac{\Delta P}{HS_{fin} - HS_{min}}, \quad (1)$$

ΔSWE was calculated for each storm interval by scaling ΔHS_{lidar} estimates by respective ρ_{new} estimates:

$$\Delta SWE = \rho_{new} \times \Delta HS_{lidar}. \quad (2)$$

The accuracy of the acoustic snow depth sensor is ±1 cm. This accuracy limitation and the assumption of spatially homogeneous fresh snow density may be reflected in the resulting ΔSWE products, but are considered minor given the small spatial variations in fresh snow density normally observed under forest canopies (Hedstrom & Pomeroy, 1998).

2.6 | Lidar canopy products

2.6.1 | Canopy radiation transmittance from voxel ray sampling of lidar

A novel lidar resampling method was developed for estimating radiation transmittance through vegetation from discrete-return lidar observations using a discrete voxel traversal and voxel-wise Bayesian inference method, referred to as voxel ray sampling of lidar (VoxRS). Occlusion of lidar beams by dense vegetation is known to result in underestimation of distal (i.e. understory, for aerial lidar) vegetation densities calculated from resulting point clouds (Béland et al., 2019; Chasmer et al., 2006), and recent efforts have been made to correct for these errors through creative methods of lidar resampling (Béland et al., 2014; Kükenbrink et al., 2016) or allometric enhancement (Webster et al., 2023). VoxRS is a resampling method motivated by the need for high angular-resolution, scalar radiation transmittance and vegetation density metrics for validation and modelling uses, which are insensitive to nonuniform lidar sampling arising from beam occlusion in vegetation, avoid explicit and computationally expensive voxel traversal (Béland et al., 2014), and which limit potential bias from the commutation and thresholding assumptions used in analysis of thresholded hemispherical images (Staines, 2021). The term radiation transmittance used hereafter refers specifically to 905 nm radiation, the wavelength of the lidar unit used in this study.

VoxRS leverages often underutilized lidar sensor trajectories in combination with the point cloud of first returns to create a voxel-wise Bayesian model of lidar return probability over the region of interest following Staines (2021). A binomial likelihood model of return probability per metre transected was created for each voxel based on observed voxel returns and sampled trajectories, combined with a beta prior (Bolstad & Curran, 2016) selected to match the mean

(μ_{prior}) and variance (σ^2_{prior}) of the observed global return probability. The posterior voxel space was then resampled along rays of interest, with a scalar correction for lidar beam specifications determined from optimization with thresholded hemispherical photography, to arrive at estimates of canopy contact numbers (χ) and radiation transmittances (T) along arbitrary rays. A maximum distance cut-off of 50 m was used to improve computational efficiency. Full documentation of the VoxRS algorithm including theoretical framework, algorithm, optimization, and sensitivity analysis are provided in the Supporting Information.

The VoxRS algorithm was run separately for both "snow-on" and "snow-off" canopy conditions, over the extent of the canopy boundary (Figure 1a) using cubic voxels with a side length of 25 cm and a ray sample length of 7.96 cm. Snow-off canopy conditions were represented by the first return point cloud from 27 May 2019, while snow-on conditions were represented by the aggregation of first return point clouds from the three survey dates within the February study period (Table 1). The resulting voxel space contained 3.01×10^8 voxels, with a total of 6.06×10^7 first returns and 2.32×10^9 samples under snow-off conditions, and 3.02×10^8 first returns and 3.99×10^9 samples under snow-on conditions. Prior parameters $\mu_{prior} = 0.0117$ and $\sigma^2_{prior} = 0.0766$ for snow-off conditions and $\mu_{prior} = 0.0104$ and $\sigma^2_{prior} = 0.0733$ for snow-on conditions were calculated from the corresponding subset of voxels with at least one sample.

VoxRS was used to generate greyscale synthetic hemispherical images at 31,123 points comprising a 25 cm square grid at 25 cm above the ground (or snow) surface across the forest plot, at ~1° angular resolution for a total of 25,445 rays per image (Figure 4c); or 792 million rays for each of the two sets of canopy conditions. Computation time for building the voxel-wise Bayesian model was approximately 226 s per 10^6 lidar returns when generated on a personal computer with an Intel i7-7500U processor. Computation time for synthetic hemispheres was approximately 4.27 s per image with the same processor when calculated in series and was parallelized for efficiency.

Several aggregate products were calculated from the snow-on and snow-off VoxRS products which are summarized in Table 2. Vertically symmetric contact number, radiation transmittance, and LAI metrics were calculated by averaging over a range of conical zenith angle footprints. Some contact numbers for zenith angles beyond 60° were under-estimated due to the max distance cut-off of 50 m (see sensitivity analysis in the Supporting Information). Mean contact numbers showed negligible sensitivity to angular resolution at 1°.

2.6.2 | Other lidar canopy metrics

Additional forest canopy metrics used to drive snow accumulation models in various studies were calculated and are shown in Table 3 for comparison. These metrics were analysed to provide context for correlations with VoxRS radiation transmittance products.

TABLE 2 Canopy metrics calculated from voxel ray sampling of lidar (VoxRS).

Symbol	Metric name	Calculation
$\chi_a^{\blacktriangle}$ $\chi_a^{\triangle}$	Contact number by angular footprint (−)	Mean contact number $\underline{\chi_i}$ for zenith angles $\phi_i \in [0°, a°)$, weighted by solid angle
$T_a^{\blacktriangle}$ $T_a^{\triangle}$	Radiation transmittance by angular footprint (−)	Mean radiation transmittance $\underline{T_i} = \underline{e^{-\chi_i}}$ for $\phi_i \in [0°, a°)$, weighted by solid angle
$LAI_a^{\blacktriangle}$ $LAI_a^{\triangle}$	Leaf area index by angular footprint (−)	Average leaf area index $\underline{LAI_i} = 2\chi_i \cos(\phi_i)$ for $\phi_i \in [0°, a°)$, weighted by solid angle
$LAI_{2000}^{\blacktriangle}$ $LAI_{2000}^{\triangle}$	LICOR LAI-2000 (−)	Leaf area index calculated by $w_i \cdot \chi_i \cdot \cos(\phi_i)$ for $\phi_i \in \{0°-15°, 15°-30°, 30°-45°, 45°-60°\}$ with respective weights $w_i = \{0.034, 0.104, 0.160, 0.702\}$ (Li-Cor., 1992)

Note: All VoxRS metrics are annotated to distinguish between snow-off ($\blacktriangle$) and snow-on ($\triangle$) canopy conditions.

2.7 | Analysis

2.7.1 | Resampling of areal snow estimates

Airborne lidar sampling of snow and ground surfaces within forests is often occluded by forest vegetation, resulting in fewer observations below dense vegetation than in gaps (Hopkinson & Chasmer, 2009). Data-sparse regions may result in unobserved pixels in digital surface models (DSMs) with increasing prevalence at higher-resolutions. Spatial interpolation is commonly used for gap filling DSMs, but interpolation can lead to bias in areal statistics when gaps systematically correspond to local extrema. For subcanopy snow surfaces, gaps in airborne lidar observations often coincide with regions of reduced snow accumulation below and around dense vegetation. There is therefore a need to assess and correct for systematic bias in areal statistics of forest snow depths calculated from airborne lidar measurements to make them representative of all regions within the forest – both observed and unobserved.

To address this, rejection sampling was used to resample the set of "observed" pixels in raster snow depth estimates to compensate for bias with vegetation density (Bolstad, 2009). A laser penetration metric considering first and last returns (LPM-L, Table 3) was selected to represent vegetation density with limited sensitivity to spatial variations in sapling density (Alonzo et al., 2015). The normalized LPM-L distribution over the set of observed pixels (O) in each snow depth raster was resampled without replacement by piecewise rejection sampling using the normalized LPM-L distribution over all pixels (G) as the target distribution. Both distributions were binned by equal quantiles of G ($n = 50$). Observed pixels within each bin

TABLE 3 Additional canopy metrics from the literature, considered in analysis with snow products.

Symbol	Metric name (units)	Description and source
CHM	Canopy crown height (m AGS)	Crown height above ground (Khosravipour et al., 2016)
DNT	Distance to nearest tree (m)	Horizontal Euclidean distance to nearest treetop, treetops classified following Khosravipour et al. (2016)
DCE	Distance to canopy edge (m)	Horizontal rectilinear distance from 2 m AGS canopy edge, using 0.1 m steps (Mazzotti et al., 2019)
LPM-L	Laser penetration metric (−) considering first and last returns	$\frac{g_F + g_L}{g_F + g_L + c_F}$ for first ground (g_F), last ground (g_L), and first canopy (c_F) returns, for scans with $\|\phi\| \le 15°$ (Alonzo et al., 2015)
MDC	Mean distance to canopy (m)	Mean distance to canopy calculated at 1.25 m AGS for 192 azimuthal directions (Moeser, Morsdorf, et al., 2015)
TGA	Total gap area (m²)	Area of the polygon made by distance to canopy vectors at 1.25 m AGS for 192 azimuthal directions (Moeser, Morsdorf, et al., 2015)

b were then randomly accepted into the resampled subset with probability:

$$r_b = m\frac{G_b}{O_b}, \tag{3}$$

where, O_b and G_b are the quantiles of the corresponding distributions found within bin b, and $m = \min_b(O_b/G_b)$ is a scaling constant to ensure that the target distribution is less than the sample distribution for all bins. The resulting subset of observed pixels yields an LPM-L distribution which is representative of all pixels, correcting for bias in areal snow depth distributions associated with snow depth and ground return density covariance with LPM-L. In the case of no significant sample bias with vegetation density, the normalized arial distributions of LPM-L for all pixels (G) and for the set of observed pixels (O) would be statistically similar, and the rejection sampling operation would yield an identity relation.

Five-centimetre-resolution SWE and ΔSWE estimates were resampled by rejection sampling prior to calculating areal statistics. Areal means and coefficients of variation were calculated for SWE and ΔSWE estimates within each of the forest and clearing plots, for each survey date. Forest SWE_f distributions from each survey were fit with lognormal distributions following Shook and Gray (1997).

2.7.2 | Variogram analysis of forest SWE and ΔSWE

Variogram analysis was conducted for all 5-cm-resolution SWE and ΔSWE estimates within the forest plot, as well as for 25-cm-resolution VoxRS aggregate radiation transmittance estimates calculated over $1°$, $15°$, $60°$ zenith-angle footprints. 1.2×10^7 random sample pairs up to 30 m apart were drawn from each variable within the forest plot following a uniform distance distribution and binned by Euclidean distance using 60 bins of 50 cm width. Relative subpixel variance is reported for snow metrics as the fraction of variance between pixels within the local 8-connected neighbourhood (or up to 7.1 cm apart) to that found between pixels 30 m apart.

2.7.3 | Correlation analysis of forest SWE and ΔSWE with canopy metrics

The strengths of monotonic relationships between snow and canopy metrics within the forest plot were assessed at 25 cm spatial resolution using Spearman's rank correlation coefficient (ρ_s, $\alpha = 0.05$). Spearman's rank was indicated due to generally nonparametric canopy metric distributions which displayed nonlinear and heteroscedastic relationships with SWE and ΔSWE estimates. Spatial correlations were calculated for forest SWE_f and ΔSWE estimates with canopy radiation transmittance along each of the 25,445 angles over the upper hemisphere, estimated using the VoxRS method. Correlations

with snow estimates were also calculated for aggregate radiation transmittance estimates calculated over zenith angle footprints ranging from $1°$ to $90°$. Finally, correlations with snow products were also calculated for the comparison canopy metrics in Table 3.

3 | RESULTS

3.1 | Areal analysis of snow and canopy structure

3.1.1 | Snow distributions

Maps of SWE at 5-cm spatial resolution were generated across the site for each survey day (e.g. Figure 5) and exhibited both small-scale effects of individual trees on local snowpack as well as larger-scale differences between the forest and clearing. Mean areal SWE_f over the forest plot increased from 38.8 to 45.2 mm over the study period, or 32%–34% of SWE_c estimated within the clearing plot (see Table 4). Coefficients of variation of forest snowpack ranged from 0.36 to 0.44 over the study period, 138%–159% of those found for the clearing snowpack. Forest SWE_f distributions (shown in Figure 6a,b) were well-described by lognormal distributions (Faria et al., 2000) for all three days ($R^2_{adj} \geq 0.99$). Root mean squared error (RMSE) of 5-cm resolution HS_{lidar} estimates with georeferenced manual measurements was 5.2 cm within the clearing ($n = 54$) and 6.5 cm within the forest ($n = 21$), across days. RMSE of 5-cm resolution SWE estimates was 10.1 mm within the clearing ($n = 25$) and 32.2 mm within the forest
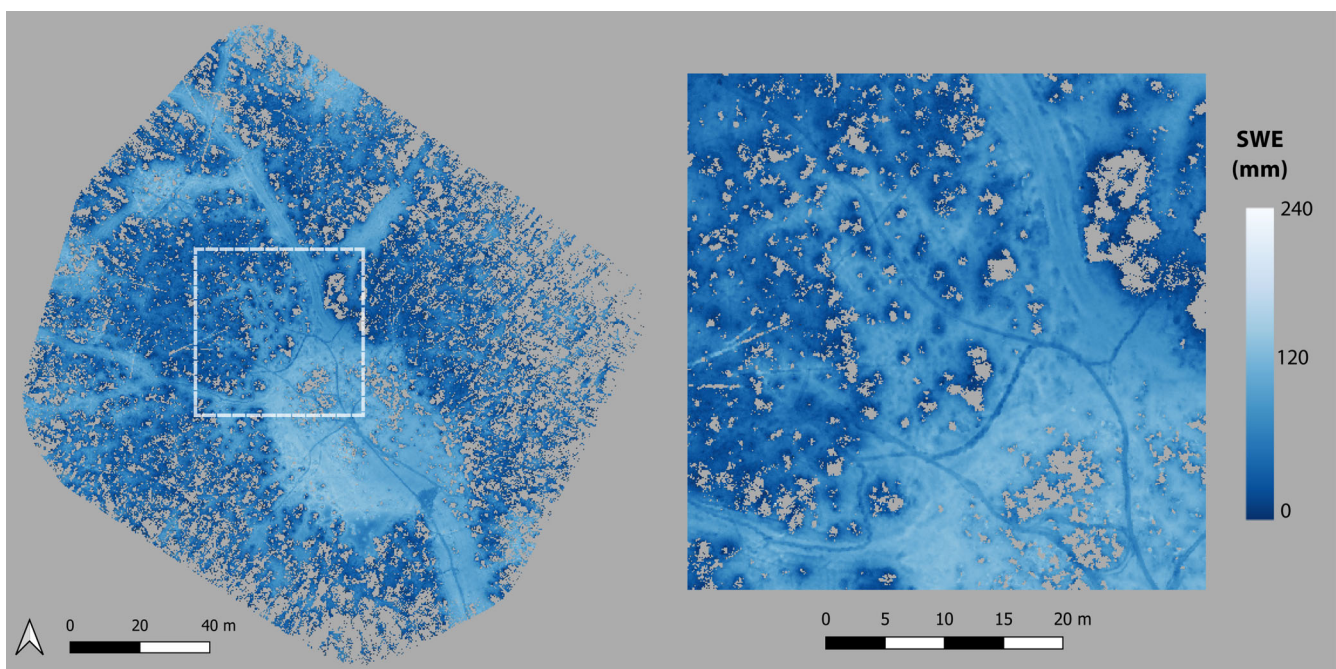
FIGURE 5 Snow water equivalent SWE_f for 19 February 2019 at 5 cm spatial resolution over the site (closeup on right). SWE maps were generated for all three survey dates using both the forest and clearing density assumptions. Gaps in observations (shown in grey) correspond to regions greater than ten horizontal cm from lidar snow depth observations. Regions of trampled snow are visible where snow surveys were conducted and were masked prior to analysis.

($n = 5$) across days, and 10.5 mm ($n = 25$) and 28.2 mm ($n = 7$) respectively at 25 cm resolution.

The mean areal ΔSWE over the forest plot was estimated at 6.4 mm for storm 1 and 3.5 mm for storm 2, or 76% and 52% of what was observed across the clearing plot (8.4 mm and 6.7 mm), respectively. Coefficients of variation were 0.89 and 0.84 for ΔSWE within
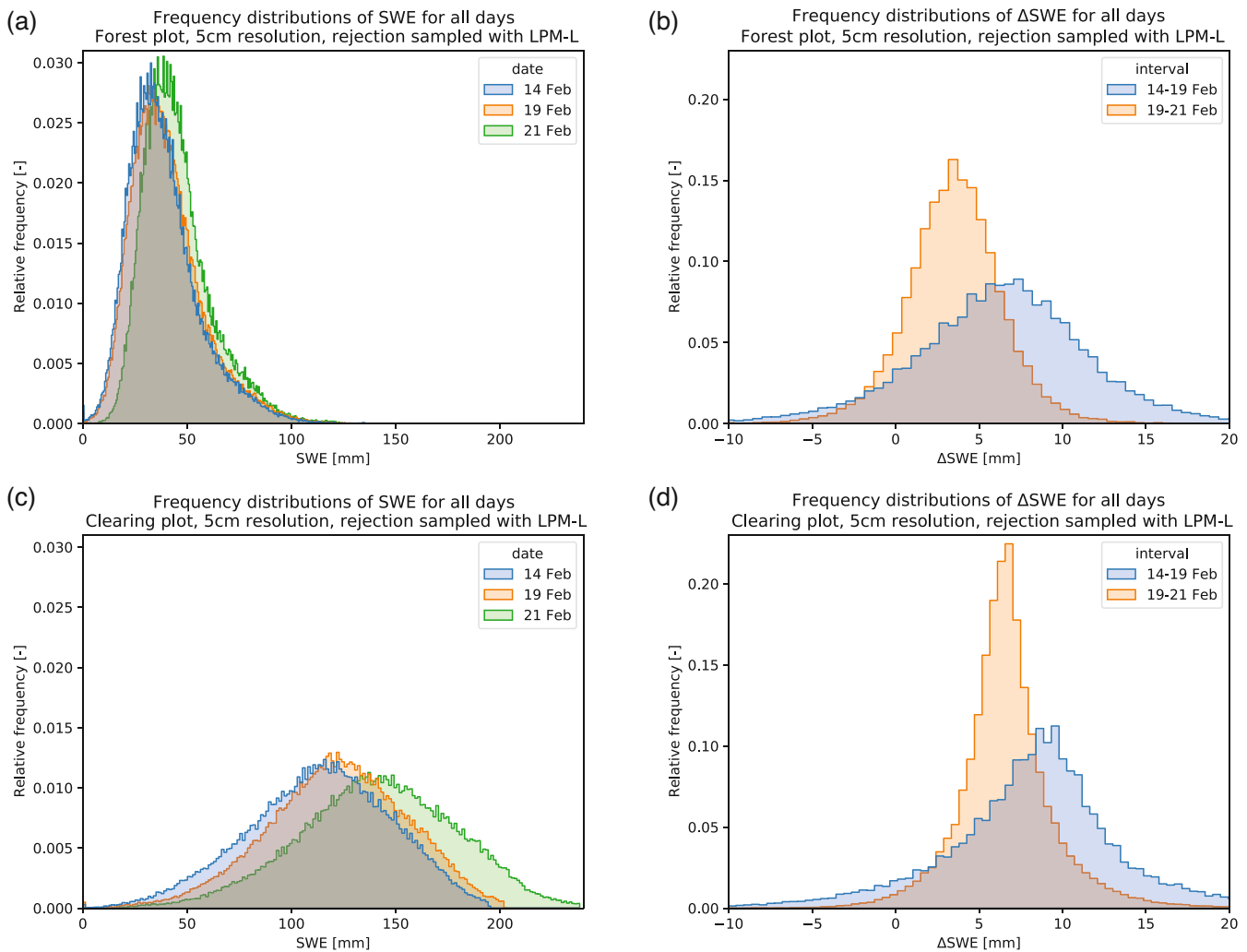
the forest and 0.73 and 0.45 for ΔSWE within the clearing, for storms 1 and 2 respectively. ΔSWE distributions for both storms are shown in Figure 6c,d, for the forest and clearing plots respectively, and highlight differences in median and spatial variation in snow accumulation between the two storms and between the forest and clearing.

3.1.2 | Forest canopy structure

Canopy radiation transmittance was modelled across the site at 25-cm spatial resolution for each of 25,445 angles across the upper hemisphere, for canopy under both snow-on and snow-free conditions, with maps such as in Figure 7 illustrating the spatial variation of canopy radiation transmittance across the site. Radiation transmittance regimes differed substantially between snow-on and snow-off conditions as seen in Figure 8, with lower median radiation transmittance in snow-on conditions for all angles compared with snow-off conditions. These observations reflect structural changes to the

TABLE 4 Areal means (μ) and coefficients of variation (c_v) of snow water equivalent (SWE) over the forest and clearing plots, calculated from 5-cm-resolution estimates corrected for sample bias with vegetation by rejection sampling.

Date	DOY	Forest SWE$_f$		Clearing SWE$_c$	
		μ (mm)	c_v (−)	μ (mm)	c_v (−)
14 February 2019	045	38.8	0.443	113	0.302
19 February 2019	050	40.4	0.431	122	0.273
21 February 2019	052	45.2	0.364	141	0.266

FIGURE 6 Distributions of (a) SWE$_f$ and (b) ΔSWE within the forest plot and (c) SWE$_c$ and (d) ΔSWE within the clearing plot, for all dates and intervals over the study period. All distributions were adjusted for sample bias by rejection sampling using the laser penetration metric LPM-L as a reference distribution.
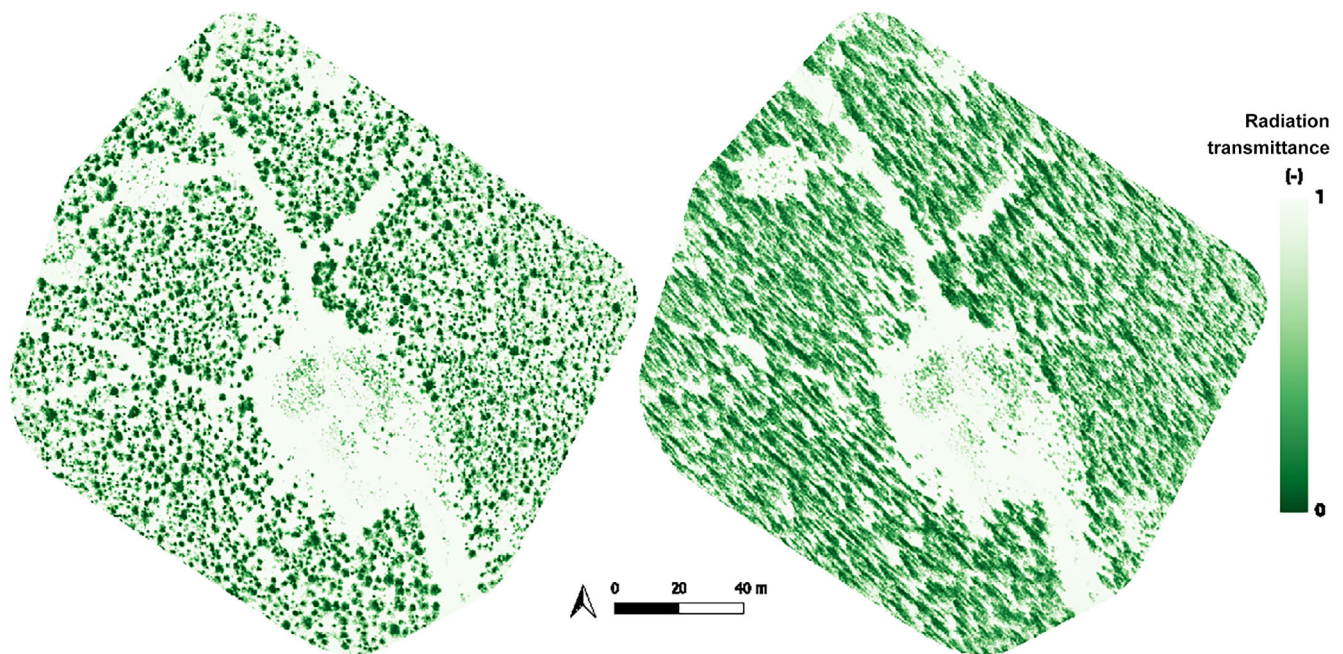
FIGURE 7 Radiation transmittance of the canopy calculated for vertical rays (left) and rays 22.5° from zenith to the southeast (right) across the site at 25 cm resolution, from VoxRS estimates under snow-free canopy conditions.
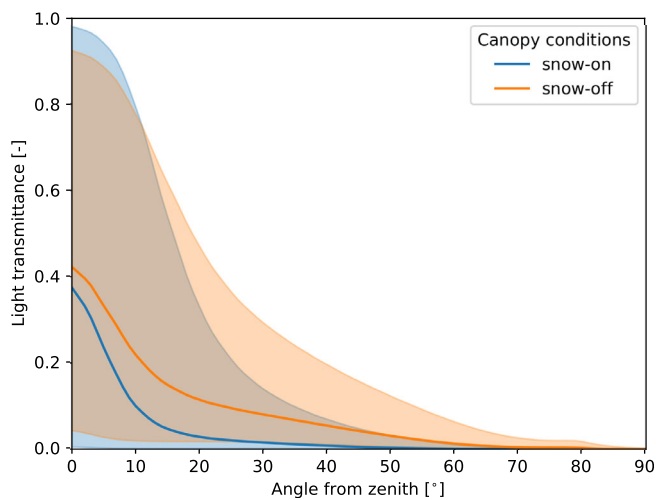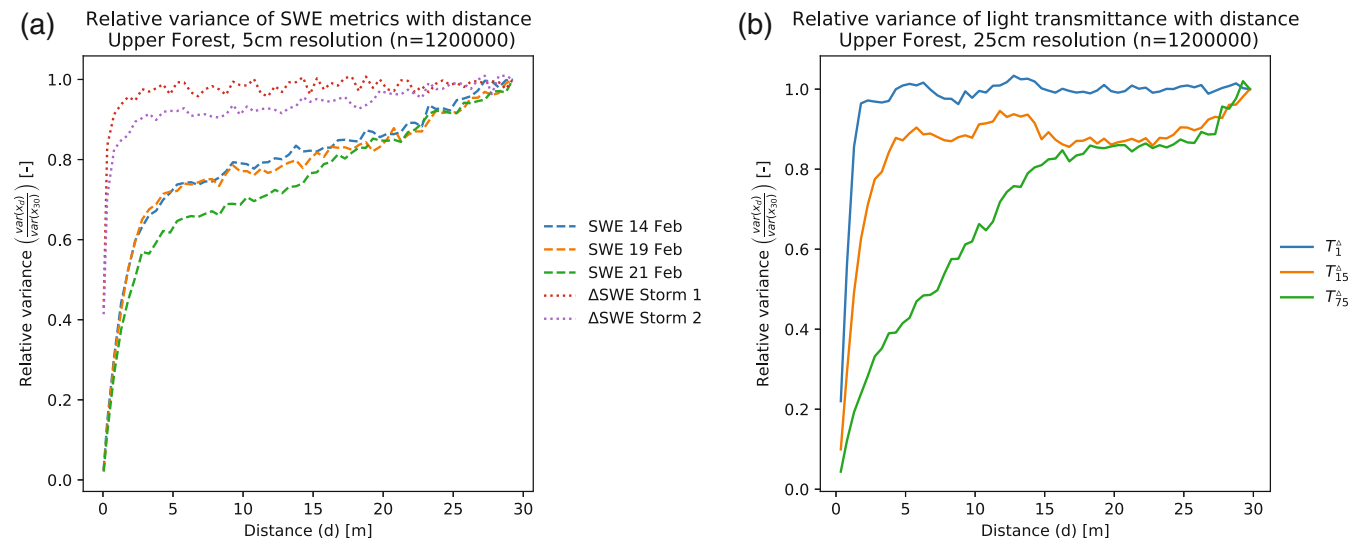

FIGURE 8 Median radiation transmittance through the forest canopy with zenith angle for snow-on (blue) and snow-off (orange) canopy conditions, with respective envelopes corresponding to interquartile ranges. Canopy radiation transmittance was estimated for 25,445 angles across the upper hemisphere at each of 31,123 points comprising a 25-cm-grid across the forest plot, and under both sets of canopy conditions using the voxel ray sampling (VoxRS) method.

and similar to findings by Webster and Jonas (2018). Median vertical radiation transmittance through the forest was 43.0% for snow-off canopy conditions compared with 39.7% for the snow-on conditions and decreased to 18.8% and 11.3% respectively for points below canopy (CHM >1 m AGS). A larger interquartile range of near-vertical radiation transmittance was seen under snow-on conditions compared with snow-free conditions (Figure 8) corresponding to branch compression from intercepted snow loads resulting in the widening of gaps between trees, and may also reflect extinction and possible multiple reflections from intercepted snow in the canopy.

3.2 | Variogram analysis of snow and canopy

Variogram analysis of forest SWE_f showed two consistent length scales of variation, with the greatest increase in variance found within 5 m of lag distance, or 63%–72% of the total variance observed at 30 m, as seen in Figure 9a. Variances continue to increase from 5 to 30 m, but at reduced rates. The standard deviation of SWE_f among neighbouring pixels at 5 cm resolution was 4.5 mm (averaged over time) corresponding to less than 3% of the variances seen at 30 m for all days. Forest ΔSWE exhibited similar length scales of variation, with a consistent scale break around 5 m. Standard deviations of ΔSWE between neighbouring 5 cm pixels for storms 1 and 2 were 5.0, and 2.6 mm, respectively, corresponding to 45.1% and 40.8% of the variance observed at 30 m lag distances. At 25 cm resolution, forest ΔSWE showed a standard deviation between neighbouring pixels of 2.0 mm, or 66.3% and 63.1% of the variance observed at 30 m for storms 1 and 2, respectively.

canopy due both to intercepted snow and the compression of branches due to the additional intercepted load. Mean LAI_{2000} over the forest plot was calculated at 5.0 under snow-off canopy conditions, and 8.2 under snow-on conditions—a substantial difference corresponding to the extent that intercepted snow changed the radiation transmittance regime of the forest canopy, consistent with Figure 8

FIGURE 9 Variance with lag distance as a fraction of variance at 30 m for sets of sampled point pairs from (a) SWE and ΔSWE products and (b) ray sampled snow-on canopy radiation transmittance metrics using 50 cm bins.
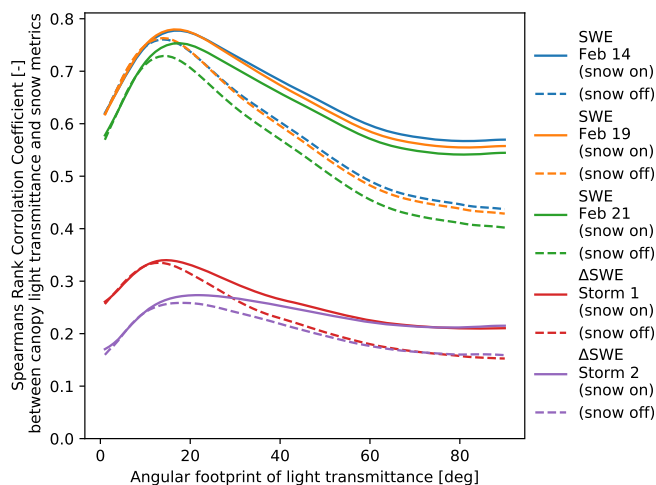
FIGURE 10 Spearman's rank correlation coefficient between snow metrics and canopy radiation transmittance across zenith angle footprints, for snow-on and snow-off conditions.

Variogram analysis of radiation transmittance under snow-on canopy conditions showed an increase in length scales of variation with increasing angular footprint as seen in Figure 9b. 50% of the 30 m variance was observed within 0.81 m of lag distance for $T_1^\triangle$, 1.35 m for $T_{15}^\triangle$, and by 7.83 m for $T_{75}^\triangle$. The variogram of $T_{75}^\triangle$ appears to reach a sill around 15 m lag distance corresponding to approximately 82% of the 30 m variance.
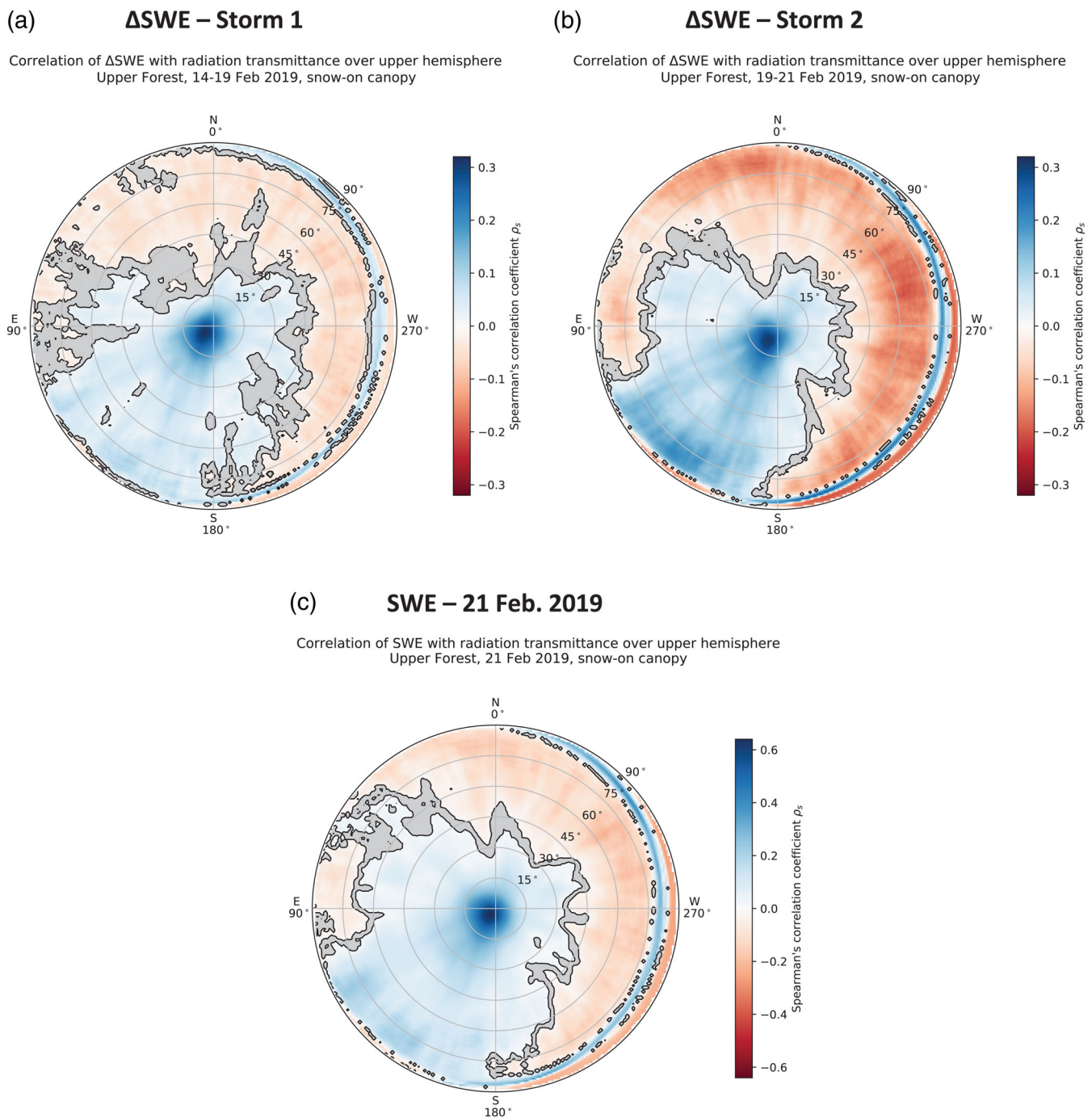
3.3 | Spatial correlations between snow and canopy

Of all canopy metrics considered, the strongest spatial correlations with SWE$_f$ and ΔSWE were found with radiation transmittance

aggregated over conical zenith angle footprints—the exception being ΔSWE over Storm 2 which had the strongest correlations with radiation transmittance at 8° from vertical to the SSE. Spearman's rank correlations coefficients (ρ_s) of forest SWE$_f$ and ΔSWE with radiation transmittance varied with the size of the conical zenith angle footprints as seen in Figure 10, with consistently stronger correlations found for radiation transmittance under snow-on canopy conditions rather than snow-off conditions. Peak correlations with SWE$_f$ ranged from 0.753 to 0.780 and were found for zenith angle footprints of 17° across all three days. ΔSWE showed peak correlations of 0.34 at 15° for Storm 1 and 0.27 at 22° for Storm 2.

Figure 11a,b shows Spearman's correlation coefficients (ρ_s) of radiation transmittance of the snow-on canopy with ΔSWE over the forest plot, for angles (zenith, azimuth) over the upper hemisphere, for storms 1 and 2. The correlations with the greatest magnitude $|\rho_s|$ within 75° from vertical were consistently positive, with values of 0.318 at (5.0°, 126.9°) for Storm 1 and 0.310 at (8.1°, 150.3°) for Storm 2. Negative correlations were generally weaker and found at greater zenith angles, with the strongest negative values being −0.10 at (75.7°, 285.3°) for Storm 1 and −0.21 at (63.8°, 283.6°) for Storm 2. Figure 11c shows ρ_s of canopy radiation transmittance with SWE$_f$ for February 21 with similar patterns to those seen with ΔSWE. Correlations were generally much stronger than for the individual storms, however, with the strongest correlation being 0.64 at (4.24°, 135.0°).

Whilst near-vertical radiation transmittance metrics showed the strongest overall correlations, LAI$_{15}$ shared the strongest correlations of the comparison metrics in Table 3 with SWE$_f$ (−0.70 to −0.73) and ΔSWE (−0.32 for storm 1, −0.25 for storm 2). Of the comparison metrics, DCE shared the next-strongest correlations with forest SWE$_f$ for all three days, with ρ_s values ranging from 0.59 to 0.62. MDC shared the next-strongest correlations with forest

(a) **ΔSWE – Storm 1**

Correlation of ΔSWE with radiation transmittance over upper hemisphere
Upper Forest, 14-19 Feb 2019, snow-on canopy

(b) **ΔSWE – Storm 2**

Correlation of ΔSWE with radiation transmittance over upper hemisphere
Upper Forest, 19-21 Feb 2019, snow-on canopy

(c) **SWE – 21 Feb. 2019**

Correlation of SWE with radiation transmittance over upper hemisphere
Upper Forest, 21 Feb 2019, snow-on canopy

FIGURE 11 Spearman's correlation coefficient (ρ_s) between snow-on radiation transmittance of the snow-on canopy and ΔSWE for (a) storm 1, (b) ΔSWE for Storm 2, and (c) SWE_f for 21 February 2019, for angles across the hemisphere. Nonsignificant values are shown in grey ($\alpha = 0.05$). Radiation transmittance was estimated at 1° angular resolution across the hemisphere over a 25-cm-grid across the forest plot. Plots are shown using the upward-facing perspective from the ground, with north to the top and east to the left.

ΔSWE for both storms (after near-vertical radiation transmittance metrics and LAI_{15}) with ρ_s values of 0.25 for Storm 1 and 0.22 for Storm 2. These findings support those of Mazzotti et al. (2019), who highlighted the need for diverse canopy metrics of limited covariance for driving snow-vegetation models. All ρ_s values for the comparison metrics in Table 3 across storms and days are provided in the Supporting Materials.

4 | DISCUSSION

Radiative transfer through the canopy is impacted by intercepted snow load across zenith angles as shown in Figure 8, with dependence on branch morphology, radiation reflection and extinction by intercepted snow clumps, and radiation frequency, among other factors. Branch deflection increases with intercepted snow load (Schmidt &

Pomeroy, 1990), yielding greater transmissivity for near-vertical rays along crown edges but reduced transmissivity within dense vegetation, culminating in greater variance in near-vertical radiation transmittance compared with snow-free conditions. This effect reverses for transmittance at lower zenith angles where branch silhouette areas generally increase with snow load, resulting in lower observed variance in transmittance beyond 15° from vertical. Intercepted snow reflects, scatters and extinguishes shortwave radiation leading to complex relationships with albedo (Pomeroy & Dion, 1996; Webster & Jonas, 2018). These combined effects result in an observed reduction in median radiation transmittance across all zenith angles with increased snow load, with the strongest differences seen at zenith angles between 5° and 40° and resulting in stronger differences in broad-angle metrics such as LAI_{2000} between the two conditions. These observations likely represent combined changes in the silhouette area of branches and reflection effects with the presence of intercepted snow and suggest promising ways forward to estimate intercepted canopy snow load by changes in canopy radiation transmittance, similar to Pomeroy and Schmidt (1993) and worthy of further investigation.

Spatial patterns of snow accumulation were related to canopy structure by nontrivial, vertically asymmetric angular footprints (Figure 11a,b) which serve as a record of snow-vegetation interactions over each accumulation period. Vertical asymmetry in angular footprints coincided with prevailing above-canopy wind directions for each of the two storms (Figure 3), consistent with the expected asymmetry of entrained snow particle trajectories. The primary source of snow particles is likely snowfall but may include net unloading of intercepted snow. Slight discrepancies between mean wind vector azimuths over the storm intervals and azimuths of peak correlations in Figure 11a,b may be due to differences in wind directions above and below the canopy due to the proximity and direction to nearby clearings (Jiao-jun et al., 2004), or discrepancies between mean wind azimuths over the storm interval compared with winds during active accumulation. Storm 2 showed greater vertical asymmetry than storm 1 coinciding with greater median and peak wind speeds compared with storm 1, further supporting windflow as the mechanism for the observed asymmetry. Similarities in angular footprints between storms and with analysis of the seasonal snowpack (Figure 11c) suggest that the asymmetry observed in the two storms is representative of snow-vegetation relationships which occurred over the snow accumulation season to date.

Near vertical throughfall and unloading explains the strongest angular relationships observed between radiation transmittance and snow accumulation, consistent with greater accumulation seen below gaps in the forest canopy (Varhola et al., 2010). These patterns are visually corroborated by comparing Figures 5 and 7, where shallow "tree wells", hollows of reduced snow accumulation, are consistently found below areas of dense vegetation. Though near vertical, these components are not explicitly vertical: the strongest correlations were deflected toward prevailing wind directions during each storm. Furthermore, substantial spreading was seen around the strongest correlations in Figure 11, corresponding to angular variation in particle trajectories within each storm interval. While modelling of near-vertical throughfall and unloading is greatly simplified by its approximation as truly vertical, ignoring vertical asymmetry or angular spread of particle trajectories is inconsistent with these observations and may be a source of bias in some cases.

While angular analysis in Figure 11 showed the strongest correlations between snowfall and radiation transmittance within 10° of vertical, significant contributions to angular footprints were found across the upper hemisphere, comprising patterns which may be explained by different snow accumulation processes. Positive correlations with radiation transmittance seen to the southeast (upwind) beyond 30° from vertical may be explained by wind gusts unloading intercepted snow and entraining falling particles along these trajectories. Additionally, significant and consistent negative correlations between radiation transmittance and snow accumulation were found beyond 30° from vertical and away from prevailing wind directions, representing greater snow accumulation at ground points with more vegetation at these downwind angles. This pattern may be a product of snow particle funnelling due to collision and rebound of snow particles from nearby branches, skewed toward windward canopy elements seeing greater collisions with entrained particles compared with sheltered lee elements. It is also possible that funnelling was introduced by inhomogeneous mean vertical wind speeds within the forest, resulting in preferential deposition of entrained snow particles independent of particle collisions with vegetation. Preferential transport of entrained particles resulting in preferential deposition has been observed and modelled for flows over terrain barriers (Comola et al., 2019) and noted across forests (Lopez-Moreno et al., 2013; López-Moreno & Latron, 2008; Mazzotti, Essery, Moeser, & Jonas, 2020; Roth & Nolin, 2017; Sanmiguel-Vallelado et al., 2020); a greater understanding of these processes at the scale of individual trees may help explain the accumulation patterns seen here. This analysis suggests that distinct snow accumulation processes may share distinct angular relationships with vegetation. Further research will help to decouple these observations to improve the independent modelling and validation of snow particle redistribution and transport processes.

While some small-scale effects of vertical asymmetry in snow-vegetation relationships can be expected to compensate for each other or average out when cumulated over large areas, there are several emergent processes illustrated in these findings which seem to be important considerations for larger-scale models. First, as snow particle trajectories deviate from vertical, their chance of traversing the canopy without collision decreases similarly to the decrease in median radiation transmittance with zenith angle (Figure 8). Radiation transmittance at the zenith angles of the strongest correlations between snowfall and radiation transmittance (5.0° for storm 1, 8.1° storm 2, see Figure 11) corresponded to 63% and 38% of the respective median vertical radiation transmittance of the snow-on canopy (Figure 8)—large changes for relatively small deviations from vertical. However, as snow particles are not intercepted by the canopy as readily as radiation is, the effects of vertical asymmetry on snow transmittance rates may be less than those for radiation transmittance, with dependence on the initial intercepted snow load

(Hedstrom & Pomeroy, 1998). As a second consideration, spatial variance of snow accumulation is expected to decrease with greater vertical deviation of snow particle trajectories, following the observed narrowing of the interquartile range of radiation transmittance of the canopy in Figure 8. Furthermore, the angular spread of particle trajectories also reduces the spatial variance of snow accumulation as the spatial effects of the canopy are blurred across many angles, which can happen over the time scales of singular or multiple storms. In this study, the combination of greater vertical deviation and greater angular spread seen for the windier Storm 2 compared with Storm 1 may explain the lower coefficients of variation seen in forest ΔSWE for Storm 2 and the lower coefficient of variation in forest SWE_f on 21 Feb. following storm 2 compared with the two previous survey dates (Table 4). These emergent processes are important for large-scale models to represent, as the spatial variance of snowpacks is one of the primary factors determining melt rates, snow cover depletion curves and contributing areas for runoff during melt periods (Faria et al., 2000; Pomeroy et al., 1998; Shook & Gray, 1996). Ongoing process- and observation-based research efforts such as by Mazzotti et al. (2023) will help to diagnose the effects of wind speed and direction on snow interception, and the resulting spatial variation of snow accumulation in forests. This improved understanding will inform further model development.

Vertically symmetric canopy metrics may not always be the best choice for parameterizing snow accumulation in forests. In this study, forest snow accumulation from both storms as well as seasonal snowpack within the forest showed stronger correlations with transmittance of off-vertical rays than with vertical rays, and were stronger than correlations with all additional canopy metrics in Table 3. Metrics with the flexibility to describe variable vertical asymmetry due to varying environmental conditions over time may more accurately represent physical interactions between snow particles and vegetation seen in this study. While the VoxRS canopy transmittance metrics used in this study may be computationally limiting for some modelling applications, directional distance to canopy metrics used to describe asymmetric relationships between snow and forest canopy resulting from solar exposure may be a more computationally convenient option for describing asymmetry in snow accumulation from wind (e.g. Mazzotti et al., 2019; Musselman et al., 2008; Webster et al., 2023).

The strongest correlations with forest SWE_f and ΔSWE in this study were found with canopy transmittance aggregated over vertically symmetric fixed-zenith-angle (i.e. conical) footprints, sensitive to the size of the angular footprint with optimal values varying across survey dates and storms (Figure 10). This suggests that such footprints are more representative of the footprint of time-averaged canopy effects on snow accumulation than any single angular projection including purely vertical, although still lacking some of the characteristics seen in the footprints in Figure 11 such as vertical asymmetry and contributions from angles with negative correlations. Canopy metrics used to parameterize snow accumulation in forests should ideally describe only the portion of canopy that is relevant for the snow particles trajectories terminating at a given point, which may

vary in time as seen in this study and in space depending on local wind patterns and proximity to terrain features. Too narrow of an angular footprint may overlook relevant nearby canopy, resulting in modelled snow distributions which vary too quickly in space. Conversely, incorporation of too wide an angular footprint that includes irrelevant distant canopy will result in modelled snow distributions which vary too slowly in space. This is reflected in the variogram analysis in Figure 9, where the 15° angular radiation transmittance shared some of the strongest correlations with SWE_f and ΔSWE (Figure 10) and had length scales of variation which more closely matched those of SWE_f and ΔSWE than did radiation transmittance over narrower or wider angular footprints. Considering spatial footprints by variogram analysis may therefore be a useful tool for matching snow-vegetation relationships with appropriate canopy metrics when angular footprint analysis is not available, or when considering the class of distance-to-canopy metrics (e.g. DCE, MDC, TGA) which describe nontrivial angular footprints of the canopy. While relationship between angular and spatial footprints of distance-to-canopy metrics generally depend on crown shape and canopy threshold height (Roth & Nolin, 2019), further research is needed to understand these relationships—to support their physical interpretations and direct comparisons with snow particle trajectories and their relationships with vegetation density across forests and conditions.

In this study, over half of the spatial variation in SWE across the forest plot was observed within distances of 2 m. Models which explicitly represent the variability of snowpack and snow accumulation within forests should therefore include resolutions well below 2 m to capture the primary spatial variations observed here, corroborating similar findings from Mazzotti et al. (2019). Models run at larger spatial scales should therefore implicitly represent or parameterise sub-grid variability in snow accumulation (Mazzotti et al., 2023). This length scale break coincides with the dominant horizontal length scale of radiation transmittance of the canopy over the 15° angular footprint relevant for falling snow particles at this site, consistent with vegetation being the primary cause of spatial variation at these scales (Trujillo et al., 2007). The strong influence of vegetation on snow accumulation is further corroborated by the significant differences in snow accumulation distributions between the clearing and forest plots, as seen in Figure 6 and throughout other forested research sites (Lopez-Moreno et al., 2013; Mazzotti et al., 2023; Roth & Nolin, 2017).

This study was conducted to closely examine spatial heterogeneity in snow accumulation within a forest. The use of Spearman's rank correlation coefficients to analyse relationships between snow and canopy metrics not only allowed for comparisons across differing nonlinear and heteroscedastic relationships, but also yielded results which were insensitive to spatially homogeneous sources of bias. This includes cm-scale vertical errors in GNSS base station georeferencing between surveys leading to bias in lidar snow depths, SWE, and ΔSWE estimates, errors in snow density models used for SWE and ΔSWE estimates, error in the optimized radiation absorption scalar used for canopy radiation transmittance estimates, and assumptions of spatially homogeneous sublimation within the forest. Variogram

analysis was similarly insensitive to these sources of bias. Spatially heterogeneous differences in fresh snow density were considered small, but may arise from unloading of intercepted snow from vegetation, and are a possible source of bias in these results.

This study assumes that pixel-wise differences in SWE estimates before and after storms are due to snow accumulation, and not a result of other processes such as ablation or wind redistribution between pixels. While some sublimation is certain, air temperatures below $-8°C$ and relative humidity near saturation throughout the study period suggest that sublimation was negligible relative to snow accumulation over the two storms. Wind speeds below a peak of 0.78 m s^{-1} within the forest over the study period were consistent with no indications of wind erosion and deposition of surface snow seen while conducting snow surveys. Furthermore, similar angular footprints of the canopy found for ΔSWE and SWE$_f$ estimates (Figure 11) suggest that the snow accumulation processes which shaped patterns of fresh snowfall from storms 1 and 2 were representative of the processes which shaped the snowpack from the beginning of the winter season through the beginning of the study.

This study pushed the boundaries of what can be measured with current UAV-lidar technology. Despite high average subcanopy surface return densities of 839 returns m^{-2}, analysis at 5 cm spatial resolution nevertheless resulted in data-sparse regions below dense vegetation which required correction for areal SWE and ΔSWE estimates. Additionally, fresh snow depths of a few cm for each storm were comparable to errors in vertical precision of the lidar setup, resulting in much greater random noise in ΔSWE estimates and lower correlations with canopy metrics compared with SWE estimates. Despite this noise, analyses of ΔSWE and SWE estimates yielded similar, statistically significant angular relationships with the canopy, illustrating the robustness of these methods.

5 | CONCLUSIONS

High resolution UAV-lidar and surface observations from two midwinter storms at a forested site revealed detailed relationships between falling snow particles and vegetation during storms, recorded in spatial patterns of sub-canopy snow accumulation. Clear effects of intercepted snow in the canopy were seen in lidar observations and canopy radiation transmittance metrics suggesting potential measurement techniques using broad angular metrics such as LAI$_{2000}$ that need further investigation. Prevailing wind direction explained the observed vertical asymmetry in angular relationships between vegetation and snow accumulation, and evidence of preferential deposition of snow due to funnelling was seen where sheltering downwind vegetation was present. These findings demonstrate that canopy and sub-canopy snowpack relationships at small length scales are sensitive to wind speed and direction during snowfall and unloading, resulting in emergent processes with important implications for how snowpack variability is characterized in larger scale snow accumulation models. Distinct contributions from different snow accumulation processes including throughfall, unloading, and funnelling were

visible in angular footprints, suggesting that the methods used here may be useful for separating these processes. Over 50% of the spatial variation in subcanopy SWE in this study was found within distances of 2 m, providing a reference length scale for delineating explicit or implicit snow accumulation models. Quantifying spatial and angular relationships between vegetation and snow accumulation informs the selection of canopy metrics which are representative of the relevant portions of canopy for realistic parametrization of snow accumulation in models. Confirmatory studies over different forests and a wider range of environmental conditions will improve our understanding of the sensitivity of snow accumulation to these variables and will inform further development of physically accurate forest snow accumulation models.

DATA AVAILABILITY STATEMENT

The data that support the findings of this study are openly available upon request. The VoxRS software is open source under the GPLv3 licence and is available at github.com/jstaines/VoxRS.

ORCID

John W. Pomeroy https://orcid.org/0000-0002-4782-7457

REFERENCES

Alonzo, M., Bookhagen, B., McFadden, J. P., Sun, A., & Roberts, D. A. (2015). Mapping urban forest leaf area index with airborne lidar using penetration metrics and allometry. *Remote Sensing of Environment*, *162*, 141–153. https://doi.org/10.1016/j.rse.2015.02.025

Andreadis, K. M., Storck, P., & Lettenmaier, D. P. (2009). Modeling snow accumulation and ablation processes in forested environments. *Water Resources Research*, *45*(5), 1–13. https://doi.org/10.1029/2008WR007042

Béland, M., Parker, G., Sparrow, B., Harding, D., Chasmer, L., Phinn, S., Antonarakis, A., & Strahler, A. (2019). On promoting the use of lidar systems in forest ecosystem research. *Forest Ecology and Management*, *450*(June), 117484. https://doi.org/10.1016/j.foreco.2019.117484

Béland, M., Widlowski, J. L., & Fournier, R. A. (2014). A model for deriving voxel-level tree leaf area density estimates from ground-based LiDAR. *Environmental Modelling and Software*, *51*, 184–189. https://doi.org/10.1016/j.envsoft.2013.09.034

Bolstad, W. M. (2009). Monte Carlo sampling from the posterior. *Understanding Computational Bayesian Statistics*, 25–46. https://doi.org/10.1002/9780470567371.ch2

Bolstad, W. M., & Curran, J. M. (2016). Introduction to Bayseian. *Statistics*, *37*, 71–75. https://doi.org/10.1080/00220973.1968.11011114

Broxton, P. D., Harpold, A. A., Biederman, J. A., Troch, P. A., Molotch, N. P., & Brooks, P. D. (2015). Quantifying the effects of

vegetation structure on snow accumulation and ablation in mixed-conifer forests. *Ecohydrology*, 8(6), 1073–1094. https://doi.org/10.1002/eco.1565

Campbell Scientific Canada. (2009). *SR50A sonic ranging sensor: Instruction manual*. Campbell Scientific Canada Corp.

Chasmer, L., Hopkinson, C., Smith, B., & Treitz, P. (2006). Examining the influence of changing laser pulse repetition frequencies on conifer forest canopy returns. *Photogrammetric Engineering and Remote Sensing*, 72(12), 1359–1367. https://doi.org/10.14358/PERS.72.12.1359

Clark, M. P., Bierkens, M. F. P., Samaniego, L., Woods, R. A., Uijlenhoet, R., Bennett, K. E., Pauwels, V. R. N., Cai, X., Wood, A. W., & Peters-Lidard, C. D. (2017). The evolution of process-based hydrologic models: Historical challenges and the collective quest for physical realism. *Hydrology and Earth System Sciences*, 21(7), 3427–3440. https://doi.org/10.5194/hess-21-3427-2017

Clark, M. P., Hendrikx, J., Slater, A. G., Kavetski, D., Anderson, B., Cullen, N. J., Kerr, T., Hreinsson, E. Ö., & Woods, R. A. (2011). Representing spatial variability of snow water equivalent in hydrologic and land-surface models: A review. *Water Resources Research*, 47(7), 8–13. https://doi.org/10.1029/2011WR010745

Comola, F., Giometto, M. G., Salesky, S. T., Parlange, M. B., & Lehning, M. (2019). Preferential deposition of snow and dust over hills: Governing processes and relevant scales. *Journal of Geophysical Research: Atmospheres*, 124(14), 7951–7974. https://doi.org/10.1029/2018JD029614

Curtis, P. G., Slay, C. M., Harris, N. L., Tyukavina, A., & Hansen, M. C. (2018). Classifying drivers of global forest loss. *Science*, 361(6407), 1108–1111. https://doi.org/10.1126/science.aau3445

DeBeer, C. M., & Pomeroy, J. W. (2010). Simulation of the snowmelt runoff contributing area in a small alpine basin. *Hydrology and Earth System Sciences*, 14(7), 1205–1219. https://doi.org/10.5194/hess-14-1205-2010

Deems, J. S., & Painter, T. H. (2006). Lidar measurement of snow depth: accuracy and error sources. In *Proceedings of the 2006 International Snow Science Workshop: Telluride, Colorado* (Vol. 330, pp. 330–338). 2006 International Snow Science Workshop.

Deems, J. S., Painter, T. H., & Finnegan, D. C. (2013). Lidar measurement of snow depth: A review. *Journal of Glaciology*, 59(215), 467–479. https://doi.org/10.3189/2013JoG12J154

Dickerson-Lange, S. E., Gersonde, R. F., Hubbart, J. A., Link, T. E., Nolin, A. W., Perry, G. H., Roth, T. R., Wayand, N. E., & Lundquist, J. D. (2017). Snow disappearance timing is dominated by forest effects on snow accumulation in warm winter climates of the Pacific northwest United States. *Hydrological Processes*, 31(10), 1846–1862. https://doi.org/10.1002/hyp.11144

Ellis, C. R., Pomeroy, J. W., & Link, T. E. (2013). Modeling increases in snowmelt yield and desynchronization resulting from forest gap-thinning treatments in a northern mountain headwater basin. *Water Resources Research*, 49(2), 936–949. https://doi.org/10.1002/wrcr.20089

Fang, X., Pomeroy, J. W., Debeer, C. M., Harder, P., & Siemens, E. (2019). Hydrometeorological data from Marmot Creek Research Basin, Canadian Rockies. *Earth System Science Data*, 11(2), 455–471. https://doi.org/10.5194/essd-11-455-2019

Faria, D. A., Pomeroy, J. W., & Essery, R. L. H. (2000). Effect of covariance between ablation and snow water equivalent on depletion of snow-covered area in a forest. *Hydrological Processes*, 14(15), 2683–2695. https://doi.org/10.1002/1099-1085(20001030)14:15<2683::AID-HYP86>3.0.CO;2-N

Golding, D. L., & Swanson, R. H. (1978). Snow accumulation and melt in small forest openings in Alberta. *Canadian Journal of Forest Research*, 8(4), 380–388. https://doi.org/10.1139/x78-057

Harder, P., Pomeroy, J. W., Helgason, W. D., & Helgason, W. D. (2020). Improving sub-canopy snow depth mapping with unmanned aerial vehicles: Lidar versus structure-from-motion techniques. *The Cryosphere*, 14(6), 1919–1935. https://doi.org/10.5194/tc-14-1919-2020

Harpold, A. A., Biederman, J. A., Condon, K., Merino, M., Korgaonkar, Y., Nan, T., Sloat, L. L., Ross, M., & Brooks, P. D. (2014). Changes in snow accumulation and ablation following the las Conchas Forest fire, New Mexico, USA. *Ecohydrology*, 7(2), 440–452. https://doi.org/10.1002/eco.1363

Harpold, A. A., Krogh, S. A., Kohler, M., Eckberg, D., Greenberg, J., Sterle, G., & Broxton, P. D. (2020). Increasing the efficacy of forest thinning for snow using high-resolution modeling: A proof of concept in the Lake Tahoe Basin, California, USA. *Ecohydrology*, 13(4), e2203. https://doi.org/10.1002/eco.2203

Hedstrom, N. R., & Pomeroy, J. W. (1998). Measurements and modelling of snow interception in the boreal forest. *Hydrological Processes*, 12(10), 1611–1625. https://doi.org/10.1002/(SICI)1099-1085(199808/09)12:10/11<1611::AID-HYP684>3.0.CO;2-4

Hopkinson, C., & Chasmer, L. (2009). Testing LiDAR models of fractional cover across multiple forest ecozones. *Remote Sensing of Environment*, 113(1), 275–288. https://doi.org/10.1016/j.rse.2008.09.012

Huerta, M. L., Molotch, N. P., & McPhee, J. (2019). Snowfall interception in a deciduous Nothofagus forest and implications for spatial snowpack distribution. *Hydrological Processes*, 33(13), 1818–1834. https://doi.org/10.1002/hyp.13439

Isenburg, M. (2020). LAStools. https://rapidlasso.com/lastools/

Jiao-jun, Z., Xiu-fen, L., Yutaka, G., & Takeshi, M. (2004). Wind profiles in and over trees. *Journal of Forestry Research*, 15(4), 305–312. https://doi.org/10.1007/bf02844959

Johnston, L. M., Wang, X., Erni, S., Taylor, S. W., McFayden, C. B., Oliver, J. A., Stockdale, C., Christianson, A., Boulanger, Y., Gauthier, S., Arseneault, D., Wotton, B. M., Parisien, M.-A., & Flannigan, M. D. (2020). Wildland fire risk research in Canada. *Environmental Reviews*, 28(2), 164–186. https://doi.org/10.1139/er-2019-0046

Khosravipour, A., Skidmore, A. K., & Isenburg, M. (2016). Generating spike-free digital surface models using LiDAR raw point clouds: A new approach for forestry applications. *International Journal of Applied Earth Observation and Geoinformation*, 52, 104–114. https://doi.org/10.1016/j.jag.2016.06.005

Kükenbrink, D., Schneider, F. D., Leiterer, R., Schaepman, M. E., & Morsdorf, F. (2016). Quantification of hidden canopy volume of airborne laser scanning data using a voxel traversal algorithm. *Remote Sensing of Environment*, 194, 424–436. https://doi.org/10.1016/j.rse.2016.10.023

Li-COR. (1992). *LAI-2000 plant canopy analyzer—Operating manual*. Li-COR, Inc.

López-Moreno, J. I., & Latron, J. (2008). Influence of canopy density on snow distribution in a temperate mountain range. *Hydrological Processes*, 22, 117–126. https://doi.org/10.1002/hyp.6572

Lopez-Moreno, J. I., Pomeroy, J. W., Revuelto, J., & Vicente-Serrano, S. M. (2013). Response of snow processes to climate change: Spatial variability in a small basin in the Spanish Pyrenees. *Hydrological Processes*, 27, 2637–2650.

Lundberg, A., & Halldin, S. (2001). Snow interception evaporation. Review of measurement techniques, processes, and models. *Theoretical and Applied Climatology*, 70(1–4), 117–133. https://doi.org/10.1007/s007040170010

Lv, Z., & Pomeroy, J. W. (2020). Assimilating snow observations to snow interception process simulations. *Hydrological Processes*, 34(10), 2229–2246. https://doi.org/10.1002/hyp.13720

Mazzotti, G., Currier, W. R., Deems, J. S., Pflug, J. M., Lundquist, J. D., & Jonas, T. (2019). Revisiting snow cover variability and canopy structure within Forest stands: Insights from airborne Lidar data. *Water Resources Research*, 55(7), 6198–6216. https://doi.org/10.1029/2019WR024898

Mazzotti, G., Essery, R., Moeser, C. D., & Jonas, T. (2020). Resolving small-scale forest snow patterns using an energy balance snow model with a one-layer canopy. *Water Resources Research*, 56, e2019WR026129. https://doi.org/10.1029/2019WR026129

Mazzotti, G., Essery, R., Webster, C., Malle, J., & Jonas, T. (2020). Process-level evaluation of a hyper-resolution forest snow model using distributed multisensor observations. *Water Resources Research*, 56(9), 1–25. https://doi.org/10.1029/2020WR027572

Mazzotti, G., Webster, C., Quéno, L., Cluzet, B., & Jonas, T. (2023). Canopy structure, topography, and weather are equally important drivers of small-scale snow cover dynamics in sub-alpine forests. *Hydrology and Earth System Sciences*, 27, 2099–2121. https://doi.org/10.5194/hess-27-2099-2023

Moeser, D., Morsdorf, F., & Jonas, T. (2015). Novel forest structure metrics from airborne LiDAR data for improved snow interception estimation. *Agricultural and Forest Meteorology*, 208, 40–49. https://doi.org/10.1016/j.agrformet.2015.04.013

Moeser, D., Stähli, M., & Jonas, T. (2015). Improved snow interception modeling using canopy parameters derived from airborne LiDAR data. *Water Resources Research*, 51(7), 5041–5059. https://doi.org/10.1002/2014WR016724

Musselman, K. N., Molotch, N. P., & Brooks, P. D. (2008). Effects of vegetation on snow accumulation and ablation in a mid-latitude sub-alpine forest. *Hydrological Processes*, 22(15), 2767–2776. https://doi.org/10.1002/hyp.7050

Musselman, K. N., Pomeroy, J. W., & Link, T. E. (2015). Variability in short-wave irradiance caused by forest gaps: Measurements, modelling, and implications for snow energetics. *Agricultural and Forest Meteorology*, 207, 69–82. https://doi.org/10.1016/j.agrformet.2015.03.014

Natural Resources Canada. (2021). Precise point positioning. https://webapp.geod.nrcan.gc.ca/geod/tools-outils/ppp.php

Newman, E. A., Kennedy, M. C., Falk, D. A., & McKenzie, D. (2019). Scaling and complexity in landscape ecology. *Frontiers in Ecology and Evolution*, 7, 1–16. https://doi.org/10.3389/fevo.2019.00293

Nilson, T. (1971). A theoretical analysis of the frequency of gaps in plant stands. *Agricultural Meteorology*, 8(1966), 25–38. https://doi.org/10.1016/0002-1571(71)90092-6

Pomeroy, J. W., & Dion, K. (1996). Winter radiation extinction and reflection in a boreal pine canopy: Measurements and modelling. *Hydrological Processes*, 10(12), 1591–1608. https://doi.org/10.1002/(SICI)1099-1085(199612)10:12<1591::AID-HYP503>3.0.CO;2-8

Pomeroy, J. W., Fang, X., & Ellis, C. (2012). Sensitivity of snowmelt hydrology in Marmot Creek, Alberta, to forest cover disturbance. *Hydrological Processes*, 26(12), 1892–1905. https://doi.org/10.1002/hyp.9248

Pomeroy, J. W., & Goodison, B. (1997). Winter and snow. In *The surface climates of Canada* (pp. 68–100). Queen's-McGill University Press.

Pomeroy, J. W., & Granger, R. (1997). Sustainability of the Western Canadian Boreal Forest Under Changing Hydrological Conditions. *Snow Accumulation and Ablation*. IAHS Publ. 240.

Pomeroy, J. W., Gray, D. M., Hedstrom, N. R., & Janowicz, J. R. (2002). Prediction of seasonal snow accumulation in cold climate forests. *Hydrological Processes*, 16(18), 3543–3558. https://doi.org/10.1002/hyp.1228

Pomeroy, J. W., Gray, D. M., Shook, K. R., Toth, B., Essery, R. L. H., Pietroniro, A., & Hedstrom, N. (1998). An evaluation of snow accumulation and ablation processes for land surface modelling. *Hydrological Processes*, 12(15), 2339–2367.

Pomeroy, J. W., & Gray, D. M. (1995) Snowcover Accumulation, Relocation and Management. *National Hydrology Research Institute Science Report No. 7*. Environment Canada, Saskatoon, Canada. 144 p.

Pomeroy, J. W., & Schmidt, R. A. (1993). The use of fractal geometry in modelling intercepted snow accumulation and sublimation. In *Proceedings of the 50th annual Eastern Snow conference* (pp. 231–239). Eastern Snow Conference.

Roth, T. R., & Nolin, A. W. (2017). Forest impacts on snow accumulation and ablation across an elevation gradient in a temperate montane environment. *Hydrology and Earth System Sciences*, 21, 5427–5442. https://doi.org/10.5194/hess-21-5427-2017

Roth, T. R., & Nolin, A. W. (2019). Characterizing maritime snow canopy interception in forested mountains. *Water Resources Research*, 55, 4564–4581. https://doi.org/10.1029/2018WR024089

Rothwell, R., Hillman, G., & Pomeroy, J. W. (2016). Marmot Creek experimental watershed study. *The Forestry Chronicle*, 92, 32–36. https://doi.org/10.5558/tfc2016-010

Rutter, N., Essery, R., Pomeroy, J. W., Altimir, N., Andreadis, K., Baker, I., Barr, A., Bartlett, P., Boone, A., Deng, H., Douville, H., Dutra, E., Elder, K., Ellis, C., Feng, X., Gelfan, A., Goodbody, A., Gusev, Y., Gustafsson, D., … Yamazaki, T. (2009). Evaluation of forest snow processes models (SnowMIP2). *Journal of Geophysical Research-Atmospheres*, 114(6), 1–18. https://doi.org/10.1029/2008JD011063

Ryan, W. A., Doesken, N. J., & Fassnacht, S. R. (2008). Preliminary results of ultrasonic snow depth sensor testing for National Weather Service (NWS) snow measurements in the US. *Hydrological Processes*, 22(15), 2748–2757. https://doi.org/10.1002/hyp.7065

Sanmiguel-Vallelado, A., López-Moreno, J. I., Morán-Tejeda, E., Alonso-González, E., Navarro-Serrano, F. M., Rico, I., & Camarero, J. J. (2020). Variable effects of forest canopies on snow processes in a valley of the central Spanish Pyrenees. *Hydrological Processes*, 34, 2247–2262. https://doi.org/10.1002/hyp.13721

Schleppi, P., Conedera, M., Sedivy, I., & Thimonier, A. (2007). Correcting non-linearity and slope effects in the estimation of the leaf area index of forests from hemispherical photographs. *Agricultural and Forest Meteorology*, 144(3–4), 236–242. https://doi.org/10.1016/j.agrformet.2007.02.004

Schmidt, R. A., & Gluns, D. R. (1991). Snowfall interception on branches of three conifer species. *Canadian Journal of Forest Research*, 21(8), 1262–1269. https://doi.org/10.1139/x91-176

Schmidt, R. A., & Pomeroy, J. W. (1990). Bending of a conifer branch at subfreezing temperatures: Implications for snow interception. *Canadian Journal of Forest Research*, 20(8), 1251–1253. https://doi.org/10.1139/x90-165

Shook, K., & Gray, D. M. (1994). Determining the snow water equivalent of shallow prairie snowcovers. In *Proceedings of the 51st eastern snow conference* (pp. 89–95). Eastern Snow Conference.

Shook, K., & Gray, D. M. (1996). Small-scale spatial structure of shallow snowcovers. *Hydrological Processes*, 10(10), 1283–1292. https://doi.org/10.1002/(SICI)1099-1085(199610)10:10<1283::AID-HYP460>3.0.CO;2-M

Shook, K., & Gray, D. M. (1997). Synthesizing shallow seasonal snow covers. *Water Resources Research*, 33(3), 419–426. https://doi.org/10.1029/96WR03532

Smith, C. D. (2007). Correcting the wind bias in snowfall measurements made with a Geonor T-200B precipitation gauge and Alter wind shield. In *Proceedings of the 7th American Meteorology Society annual meeting*. American Meteorology Society.

SPH Engineering. (2020). *Universal ground Control Station (UgCS) software, version 3.4*. SPH Engineering.

Staines, J. (2021). Spatial relationships between trees and snow in a cold regions montane forest. Unpublished MSc. Thesis, Dept. of Geography & Planning, University of Saskatchewan. https://harvest.usask.ca/handle/10388/13674

Thimonier, A., Sedivy, I., & Schleppi, P. (2010). Estimating leaf area index in different types of mature forest stands in Switzerland: A comparison of methods. *European Journal of Forest Research*, 129(4), 543–562. https://doi.org/10.1007/s10342-009-0353-8

Troendle, C. A., & Leaf, C. F. (1981). Effects of timber harvest in the snow zone on volume and timing of water yield. *Interior West Watershed Management*, 231–243. Cooperative Extension, Washington State University.

Trujillo, E., Molotch, N. P., Goulden, M. L., Kelly, A. E., & Bales, R. C. (2012). Elevation-dependent influence of snow accumulation on forest greening. *Nature Geoscience*, 5(10), 705–709. https://doi.org/10.1038/ngeo1571

Trujillo, E., Ramírez, J. A., & Elder, K. J. (2007). Topographic, meteorologic, and canopy controls on the scaling characteristics of the spatial distribution of snow depth fields. *Water Resources Research*, *43*(7), 1–17. https://doi.org/10.1029/2006WR005317

Varhola, A., & Coops, N. C. (2013). Estimation of watershed-level distributed forest structure metrics relevant to hydrologic modeling using LiDAR and Landsat. *Journal of Hydrology*, *487*, 70–86. https://doi.org/10.1016/j.jhydrol.2013.02.032

Varhola, A., Coops, N. C., Weiler, M., & Moore, R. D. (2010). Forest canopy effects on snow accumulation and ablation: An integrative review of empirical results. *Journal of Hydrology*, *392*(3–4), 219–233. https://doi.org/10.1016/j.jhydrol.2010.08.009

Volney, W. J. A., & Fleming, R. A. (2000). Climate change and impacts of boreal forest insects. *Agriculture, Ecosystems and Environment*, *82*(1–3), 283–294. https://doi.org/10.1016/S0167-8809(00)00232-2

Webster, C., Essery, R., Mazzotti, G., & Jonas, T. (2023). Using just a canopy height model to obtain lidar-level accuracy in 3D forest canopy shortwave transmissivity estimates. *Agricultural and Forest Meteorology*, *338*, 109429. https://doi.org/10.1016/j.agrformet.2023.109429

Webster, C., & Jonas, T. (2018). Influence of canopy shading and snow coverage on effective albedo in a snow-dominated evergreen needleleaf forest. *Remote Sensing of Environment*, *214*, 48–58. https://doi.org/10.1016/j.rse.2018.05.023

Zheng, Z., Kirchner, P. B., & Bales, R. C. (2015). Orographic and vegetation effects on snow accumulation in the southern Sierra Nevada: A statistical summary from LiDAR data. *Cryosphere Discussions*, *9*(4), 4377–4405. https://doi.org/10.5194/tcd-9-4377-2015

SUPPORTING INFORMATION

Additional supporting information can be found online in the Supporting Information section at the end of this article.